Simulation of the Martian dust cycle with the GFDL Mars GCM

Shabari Basu and Mark I. Richardson
Division of Geological and Planetary Sciences, California Institute of Technology, Pasadena, California, USA

R. John Wilson
Geophysical Fluid Dynamics Laboratory, National Oceanic and Atmospheric Administration, Princeton, New Jersey, USA

Received 29 January 2004; revised 26 August 2004; accepted 16 September 2004; published 24 November 2004.

[1] The Martian seasonal dust cycle is examined with a general circulation model (GCM) that treats dust as a radiatively and dynamically interactive trace species. Dust injection is parameterized as being due to convective processes (such as dust devils) and model-resolved wind stresses. Size-dependent dust settling, transport by large-scale winds and subgrid scale diffusion, and radiative heating due to the predicted dust distribution are treated. Multiyear Viking and Mars Global Surveyor air temperature data are used to quantitatively assess the simulations. Varying the three free parameters for the two dust injection schemes (rate parameters for the two schemes and a threshold for wind-stress lifting), we find that the highly repeatable northern spring and summer temperatures can be reproduced by the model if the background dust haze is supplied by either convective lifting or by stress lifting with a very low threshold and a low injection rate. Dust injection due to high-threshold, high-rate stress lifting must be added to these to generate spontaneous and variable dust storms. In order to supply the background haze, widespread and ongoing lifting is required by the model. Imaging data provide a viable candidate mechanism for convective lifting, in the form of dust devils. However, observed nonconvective lifting systems (local storms, etc.) appear insufficiently frequent and widespread to satisfy the role. On the basis of the model results and thermal and imaging data, we suggest that the background dust haze on Mars is maintained by convective processes, specifically, dust devils. Combining the convective scheme and high-threshold stress lifting, we obtain a "best fit" multiyear simulation, which produces a realistic thermal state in northern spring and summer and, for the first time, spontaneous and interannually variable global dust storms. *INDEX TERMS:* 6225 Planetology: Solar System Objects: Mars; 5445 Planetology: Solid Surface Planets: Meteorology (3346); 5409 Planetology: Solid Surface Planets: Atmospheres—structure and dynamics; 3319 Meteorology and Atmospheric Dynamics: General circulation; 0305 Atmospheric Composition and Structure: Aerosols and particles (0345, 4801); *KEYWORDS:* climate, dust, Mars

Citation: Basu, S., M. I. Richardson, and R. J. Wilson (2004), Simulation of the Martian dust cycle with the GFDL Mars GCM, *J. Geophys. Res.*, *109*, E11006, doi:10.1029/2004JE002243.

1. Introduction

[2] Atmospheric dust is a very important component of the Martian climate system. The suspended mineral aerosol interacts with both visible and infrared radiation, and through this interaction, modifies atmospheric heating rates [*Gierasch and Goody*, 1968; *Kahn et al.*, 1992]. A rich potential for feedback exists due to the nonlinear relationship between the dust distribution, heating rates, and the atmospheric circulation that transports dust. The most dramatic example of such feedback is the Martian global dust storm, which over a matter of weeks can completely enshroud the planet with haze [*Leovy et al.*, 1972; *Briggs et al.*, 1979; *Martin and Richardson*, 1993; *Smith et al.*, 2002]. Of likely equal or greater importance for the mean climate of Mars is the control of the perpetual, but seasonally varying, "background" haze of dust. Models suggest that this haze produces at minimum roughly 5–10K of warming in midlevel air temperatures compared to a clear atmosphere. The means by which this haze is maintained is unknown, but it now seems unlikely that it is maintained by slow fallout of dust following global dust storms: the high degree of repeatability of air temperatures in northern spring and summer [*Richardson*, 1998; *Clancy et al.*, 2000; *Liu et al.*, 2003; *Smith*, 2004] contrasts sharply with the interannual variability of global storms.

[3] The seasonal cycle of dust has been observed in a number of ways. Air temperatures have been measured from orbit discontinuously since 1971 [*Hanel et al.*, 1972; *Martin*, 1981; *Conrath et al.*, 2000; *Liu et al.*, 2003; *Smith*, 2004]. These data provide a powerful and highly quantita-

0148-0227/04/2004JE002243$09.00

tive constraint on the dust cycle, but one that is convolved with the seasonal cycle of insolation. Dust opacities have been directly measured from these same orbital platforms [*Martin*, 1986; *Fenton et al.*, 1997; *Smith et al.*, 2001; *Liu et al.*, 2003; *Smith*, 2004] and for more limited periods from the ground [*Colburn et al.*, 1989; see also *Toigo and Richardson*, 2000; *Smith and Lemmon*, 1999]. Germane to the issue of dust injection to support this annual cycle of haze are orbiter imaging of dust storms and dust devils. Local and regional dust storms have been observed from the Viking Orbiter camera [*Briggs et al.*, 1979], and most recently from the Mars Global Surveyor (MGS) Mars Orbiter Camera (MOC) [*Cantor et al.*, 2001]. The coverage and resolution of MOC is such that the catalog of local and regional storms provided by *Cantor et al.* [2001] now provides a good climatology for a limited portion of one year. Dust devils have been observed in Viking Orbiter images [*Thomas and Gierasch*, 1985], Mars Pathfinder meteorological and imaging data [*Murphy and Nelli*, 2002; *Metzger et al.*, 1999; *Ferri et al.*, 2003], and MOC images [*Malin and Edgett*, 2001; *Cantor et al.*, 2002; *Fisher et al.*, 2002].

[4] Dust is included in all modern numerical models of the Martian atmosphere, but usually as a prescribed opacity. This opacity is either held constant over the course of a given simulation [*Haberle et al.*, 1993, 2003] or prescribed to vary as a fixed function of season [*Forget et al.*, 1999]. Such approaches are valuable as they allow the dust to be controlled as a free parameter when investigating a variety of atmospheric phenomena. However, these approaches are obviously very limiting when it comes to examining the dust cycle itself. Interactive dust experiments, which involve the coupling between the modeled winds, the dust distribution, and the calculation of atmospheric radiative heating rates were first undertaken in General Circulation Models (GCM) in the mid-1990s [*Murphy et al.*, 1990; *Wilson*, 1997]. These studies were directly focused on the simulation of forced global dust storms and resulting polar warming phenomena; prescribed surface sources of dust were used to trigger the storms. Annual and interannual GCM simulations described by *Fenton and Richardson* [2001], *Richardson and Wilson* [2002], and *Richardson et al.* [2002] used interactive dust with an injection scheme based on surface-atmosphere temperature differences to simulate the seasonal cycle of non-dust-storm opacities and air temperature, performing well in comparison with observations [*Richardson and Wilson*, 2002]. However, simulation of large dust storms has remained the key focus of GCM dust studies to the present time. Most recently, *Newman et al.* [2002a, 2002b] implemented a set of interactive dust injection parameterizations, allowing interactions between the circulation, radiative environment, and dust injection to be examined for the first time. Critically, this allowed dust injection and dust storms to be generated as prognostic, ''emergent'' features of each simulation (in contrast to the ''forced'' nature of previous studies). The *Newman et al.* [2002b] simulations generated storms similar to the 1999 ''flushing storm'' event observed by MGS [*Cantor et al.*, 2001; *Smith et al.*, 2001; *Liu et al.*, 2003], likely due to the mechanism described by *Wang et al.* [2003].

[5] In future papers describing our studies, the dynamics of global dust storms and their interannual variability will be a major focus. However, in order to generate meaningful simulations of global dust storms, we believe it is crucial to properly simulate the ''background'' state from which these storms are spawned. The reason for this, as described further in a companion paper (S. Basu et al., manuscript in preparation, 2004) (hereinafter referred to as B04), is that the background dustiness of the atmosphere strongly mediates the response of the atmospheric circulation to a given amount of injected dust, as would be expected as a possible outcome for such a complex nonlinear system. This means that one could develop major storms too easily, or with too great a difficulty if the background state of the model is incorrectly (unrealistically) defined. Conversely, generation of a global dust storm in southern summer is meaningless if as a natural consequence of the required dust injection parameters, the model generates global dust storms in northern summer, which is inconsistent with observations [*Newman et al.*, 2002b].

[6] Aside from its control of dust storm genesis, the seasonally varying haze is a critical component of climate on Mars, moderating mean air temperatures and the corresponding circulation. Attaining understanding of the mechanisms controlling this cycle is critical if we are to examine how Martian climate may have differed in the past when forced by different patterns of insolation (such as associated with changes in obliquity [*Kieffer and Zent*, 1992]). Despite its direct and indirect importance, relatively little effort has been expended directly studying the ''background'' seasonal cycle of dust and hence air temperatures without prescription. This paper focuses on this cycle.

[7] This study takes advantage of dust injection parameterizations inspired by those developed and used by *Newman et al.* [2002a]. These schemes focus on two injection mechanisms: lifting by convective processes (based on a thermodynamic theory of dust devils), and lifting directly related to the model resolved winds. These schemes are still quite primitive in the sense that their scale dependence has not been exhaustively studied. As such, we see this work as a first explorative step. In this light, we use only three free parameters to control the schemes, with the hope that the scale dependence is folded into these constants. As described in section 3, these free parameters are injection rate coefficients applied to convective and wind stress lifting, and a stress-threshold for wind stress lifting. We have extensively explored the phase-space of these free parameters, simultaneously targeting a realistic background (non-dust-storm) climate and generation of realistic global dust storms. Realism in the former case is tested through the use of observed global air temperatures as a quantitative constraint. Realism in this latter case is defined as generation of spontaneous and interannually variable global dust storms in southern spring and summer (and not in northern spring and summer). The twin requirements of continuous haze and distinctly noncontinuous dust storm generation places constraints on the model dust injection parameters that would not be in force if either requirement were imposed alone. The solution that arises in the model is that while stress lifting could create either a background haze or global storms, it cannot do both simultaneously with the same injection parameters. Conversely, dust devil injection cannot generate spontaneous and variable storms regardless of the rate coefficient value.

As a result, an idea that emerges in this paper, is one of a natural separation between the roles of convective and wind stress lifting. However, it seems plausible that convective lifting is not important and that two or more different sets of stress-lifting parameter values could be used simultaneously instead. We examine both hypotheses in light of available observations, which appear to favor convective (and specifically dust devil) supply over supply by local dust storms or other wind stress related lifting.

[8] In this paper, we provide a brief introduction to the observational constraints, and then proceed to describe the Geophysical Fluid Dynamics Laboratory (GFDL) Mars GCM, and the dust lifting schemes specifically added for this study. The model is then used to explore the areas of phase space wherein a realistic cycle of background dust opacity (as gauged by the air temperatures) is obtained. The results of our experiments suggest that a steady (yet slowly, seasonally varying) and widespread source is necessary. This widespread and persistent source can be generated by convective or wind stress driven sources. We will argue that observational constraints favor the convective source, in the form of widespread dust devil activity, though this is not conclusive, and further effort needs to be applied to observationally constrain the roles of the potential steady and widespread sources. In the latter part of this paper, we pick a set of dust lifting parameters that provide a "best fit" to the seasonal air temperature cycle, and that also yield interannually variable, spontaneous global dust storms in southern spring and summer. The non-dust-storm seasonal cycle of this simulation is examined in detail and compared with observations. Finally, we look at the patterns of net dust lifting generated by this model for current orbital parameters. These simulations provide by far the best model estimates of net dust lifting/deposition to date since the model uses a fully interactive dust cycle and this cycle has been strongly constrained by the thermal observations.

2. Observations

[9] The temperature and dust opacity of the Martian atmosphere has been monitored telescopically and by spacecraft for a substantial portion of the past several decades [*Hanel et al.*, 1972; *Martin and Kieffer*, 1979; *Martin*, 1981, 1986; *Colburn et al.*, 1989; *Clancy et al.*, 1990, 1996, 2000; *Martin and Zurek*, 1993; *Martin and Richardson*, 1993; *Fenton et al.*, 1997; *Smith et al.*, 2001, 2002; *Liu et al.*, 2003; *Smith*, 2004]. The behavior of the atmosphere can be summarized in terms of the global-mean, midlevel air temperatures derived from the Viking IRTM and synthesized from Mariner 9 and MGS Thermal Emission Spectrometer (TES) data. Midlevel in this context refers to a region between roughly 10 km and 40 km altitude, with a maximum weighting on values at ~25 km. The weighting function is shown in Figure 1 of *Wilson and Richardson* [2000] and corresponds to the spectral response function of the IRTM 15-μm channel, which is situated on the vibrational-rotational band of CO_2 gas. Brightness temperatures from this channel (or synthesized from other instruments through application of this response function) are often referred to as T15. The T15 data (Figure 1) show a cycle with minimum temperatures in late northern spring, and maximum temperatures during southern spring and summer. The spikes in the data that occur predominantly in southern spring and summer are regional and global dust storms. The combined Mariner 9, Viking, and MGS data record, from which Figure 1 is taken, is more thoroughly described and discussed by *Liu et al.* [2003]. The repeatability of the cycle throughout northern spring and summer allows a climatological mean temperature cycle to be meaningfully defined. In our case, this climatology is constructed as a "by-eye" fit to the data: in fact, any number of complex techniques could be used to fit curves to the data, with effectively no impact on the utility and accuracy of the resulting product for our application. This climatology is obviously of much less validity in southern summer; we have chosen to define it as a smooth function, which non-dust-storm temperatures in southern summer relax to. This climatology will be used to guide numerical simulations later in this paper. Cross sections of temperature retrieved from TES [*Conrath et al.*, 2000] data provide a more complete constraint on the simulations. The TES data will be used for comparison with the model at particular instants in the seasonal cycle.

[10] Imaging provides a nonquantitative but critical data set for this study. We use these data in the form of condensed summaries [*Cantor et al.*, 2001; *Fisher et al.*, 2002] to constrain the distribution and nature of small-scale dust lifting events.

3. Model

[11] The GFDL Mars GCM is a Mars-adapted version of the GFDL Skyhi GCM [*Hamilton*, 1995; *Wilson and Hamilton*, 1996]. The model has been described in various papers used to study Martian thermal tides [*Wilson and Hamilton*, 1996; *Wilson and Richardson*, 2000; *Wilson*, 2000; *Hinson and Wilson*, 2004], surface winds [*Fenton and Richardson*, 2001], the water cycle [*Richardson and Wilson*, 2002; *Richardson et al.*, 2002], transient waves and cyclones [*Hinson and Wilson*, 2002; *Wilson et al.*, 2002; *Wang et al.*, 2003], and Martian paleoclimate [*Mischna et al.*, 2003]. Briefly, the model provides a grid point representation of the global atmosphere from the surface to roughly 85 km altitude. In this paper, a horizontal grid point spacing of 5° in latitude and 6° longitude is used, with 20 vertical levels of nonuniform thickness. The model includes treatment of: the CO_2 cycle, with prognostic seasonal variations in surface pressure and seasonal ice cap extent; the water cycle, with transport of atmospheric water vapor and ice, and exchange with surface water ice deposits; radiative interactions in the visible and thermal infrared with dust and CO_2 gas; topography derived from Mars Orbiter Laser Altimeter gridded data; and calculation of surface temperatures using a 12-layer subsurface model and surface energy balance including the effects of measured albedo and thermal inertia.

[12] The model includes transport of dust resulting from advection by the model-resolved winds, horizontal and vertical subgrid-scale diffusion, and size-dependent sedimentation. As mentioned above, the instantaneous dust distribution is used within the model radiation subroutine to determine the solar and thermal infrared heating/cooling due to dust. Two different particle sizes are treated to provide a minimal representation of particle size distribution

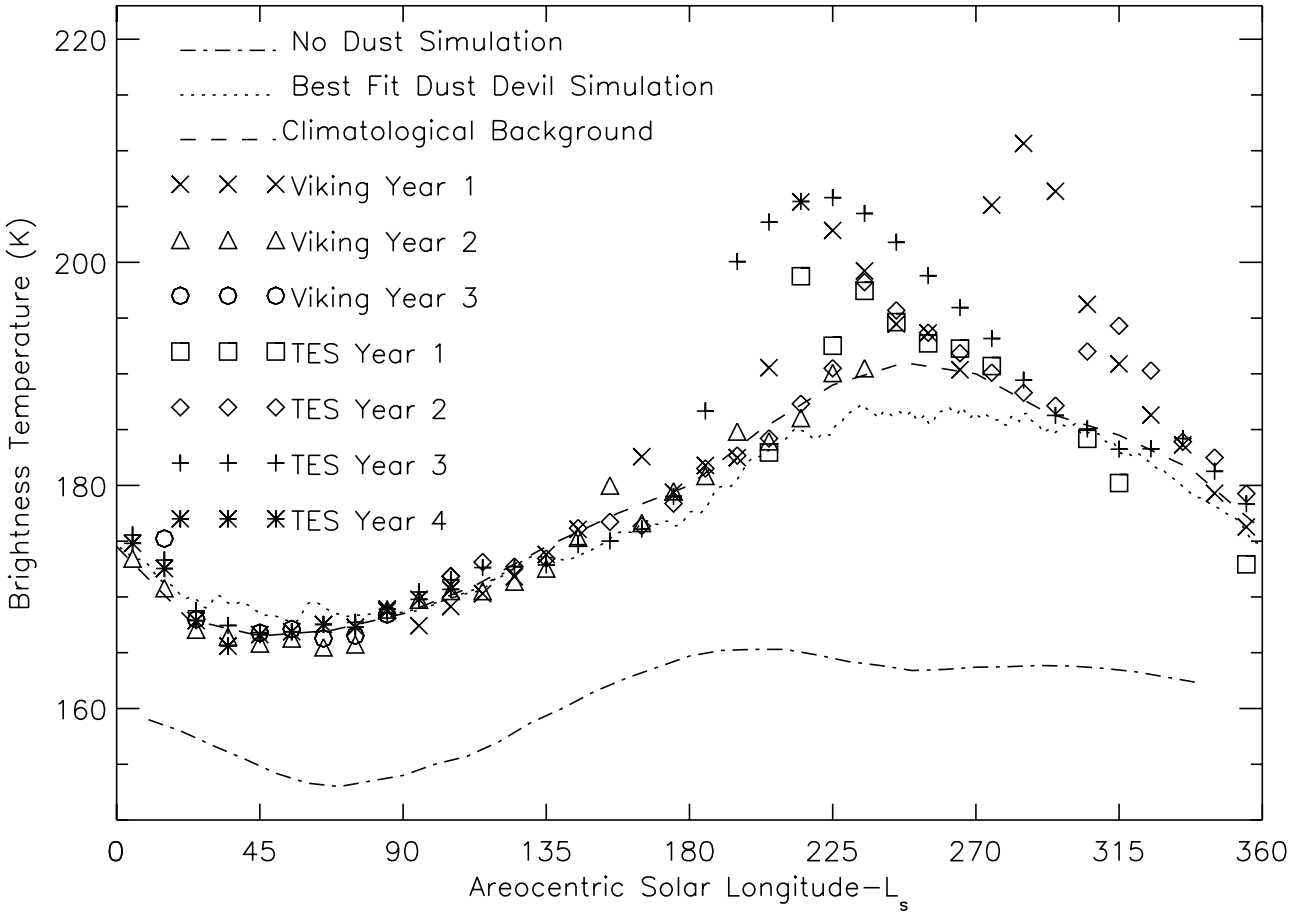

Figure 1. The seasonal variation of midlevel atmospheric temperatures between 40°S and 40°N derived from spacecraft infrared observations and from selected GCM simulations. The data are taken from the Viking Infrared Thermal Mapper (IRTM) 15-μm channel (corrected [see *Wilson and Richardson*, 2000; *Liu et al.*, 2003]) and from the Mars Global Surveyor Thermal Emission Spectrometer (TES) spectra after convolution with the IRTM 15-μm channel spectral response function. The corresponding IRTM 15-μm channel weighting function peaks at roughly 25 km, with contribution primarily from 10 to 40 km. This weighting function has been applied to the GCM output for optimal comparison with data. A mean seasonal climatology of air temperature (the "background cycle," which excludes large dust storm effects) has been defined via a "by-eye" fit to the observations. GCM simulations corresponding to the "best fit" dust devil source, and a simulation with no atmospheric dust opacity. The background haze generates about 5–10K of warming compared to a clear atmosphere. Note that the minima near the solstices correspond to the relative deposition of more solar heating poleward of 40° at these seasons than during the equinoxes.

changes. The radiation scheme treats dust as an absorbers and scatterers in the visible (with a single scattering albedo of 0.92). In the thermal infrared, only absorption and emission are considered (see *Wilson and Hamilton* [1996], and note that in some versions of the GFDL model, a more detailed radiative scheme has been used [*Hinson and Wilson*, 2004]). Using fixed dust distributions or finely tuned interactive dust injection, it has proven possible to simultaneously fit air temperatures and observed TES dust opacities.

[13] The new components of the model for this study relate to dust injection. Dust injection in the real Martian atmosphere takes place in association with motions on a variety of scales, running the gamut from synoptic motions to those associated with boundary layer turbulence. Obviously, this full spectrum cannot be explicitly treated in a model with grid spacing of order hundreds of kilometers. We therefore are faced with choices about how we parameterize lifting processes that are not model resolved. Imaging observations suggest that dust lifting is at least sensitive to the "mean wind" (on some scale) and to convective motions. The former is indicated, for example, by dust streaks and the latter by dust devils captured in spacecraft images [e.g., *Fenton and Richardson*, 2001; *Cantor et al.*, 2002]. On this basis, it seems plausible to base lifting around schemes that are related to the strength of the resolved wind (or actually the imparted stress) and the vigor of boundary layer convection. This is not necessarily unique; on the mesoscale and microscale, the "mean wind" can be modified by local topography and surface thermal contrasts such that a number of different stresses are

working within a single GCM grid cell. It again seems plausible that these subresolved winds would scale with the strength of the grid-resolved mean wind, but it is not necessarily so (profoundly nonlinear acceleration processes can be at work in some circumstances [*Magalhaes and Young*, 1995]). A detailed mesoscale modeling study is necessary to address the importance of microscale and mesoscale influences on "mean wind" dust lifting. In any case, for our initial study of the Martian dust cycle, it would seem to be prudent to devise parameterizations that represent some dependence on mean winds and on convective vigor, while at the same time, keeping the schemes sufficiently simple that they can readily be comprehended. No doubt more complex and realistic schemes will emerge in the future; their impact in changing the results of this study (or not) will be of great importance for developing an increasingly complete understanding of the Martian dust cycle.

[14] The two schemes used in this paper are inspired by those first implemented in a GCM by *Newman et al.* [2002a, 2002b]. The first relates lifting to the model-resolved wind via relationships worked out in wind tunnel experiments [e.g., *Shao*, 2001]. The second uses the *Renno et al.* [1998] thermodynamic theory of dust devils as the basis for predicting convective lifting. The representations of lifting are incomplete in that there is no scale dependence (no explicit dependence on grid spacing) such that the schemes need to be adjusted for model runs with different resolution. Our experience suggests that the stress scheme requires larger-scale correction than does the convective scheme. In any case, parameterizations in the future should account for resolution variations. More importantly, we have intentionally chosen to take only the functional forms for the lifting schemes from wind tunnel results and from theory: We have chosen to use free parameters to scale the functions as an active part of our experiments. We feel this is an honest reflection of our ignorance of the microscale processes involved in dust lifting. Tunable free parameters allow us to sidestep this ignorance (or rather contain this ignorance within a parameter, whose meaning may be examined at some later time). The connection to reality is provided by well-known constraints: the large-scale atmospheric temperatures and the functional forms of the lifting parameterizations that are based on the observed physics. In the next two subsections, we describe these parameterizations.

3.1. Convective ("Dust Devil") Parameterization

[15] The parameterization of small-scale convective motions is based on thermodynamic theory of dust devils [*Renno et al.*, 1998]. This choice is rooted in our bias that dust devils are likely the dominant form of convective lifting (not proven and in need of observational testing). However, this choice is actually quite general and reasonable since the functional form relates lifting to the stability of the boundary layer and the vigor of heat transfer between the surface and the atmosphere: more generally, the scheme links lifting to the strength of convective motions and as such should capture the nature of any convective lifting.

[16] The convective scheme (hereinafter generally referred to as the dust devil lifting or DDL scheme) is implemented using a simple fixed function that is based on the thermodynamics of dust devils [*Renno et al.*, 1998]. The *Renno et al.* [1998] heat engine theory of dust devils relates the dust lifting intensity to the sensible heat input, F_{heat}, at the surface and the thermodynamic efficiency, η, which depends on the depth of the Planetary Boundary Layer (PBL). The lifting rate is then related to the intensity with the application of a multiplicative injection rate constant, R_{DDL}. This free parameter allows for potential (and likely) offsets between the lifting of a single dust devil responding to a local heat flux and thermodynamic efficiency, and that of an ensemble of dust devils responding to a range of local environments within a model grid box of roughly 300 km width, and with grid-average values of sensible heat flux and thermodynamic efficiency. Since this multiplier is unknown a priori, we use it as one of the available tuning parameters in the model, with the seasonal cycle of air temperatures defining the "target" for tuning, as described later in this paper. The dust devil injection function is specifically defined as

$$F_{DDL} = R_{DDL} \times F_{heat} \times \eta.$$

The dust injection rate scheme is implemented in the GCM such that, so long as the function is positive at a given grid point, there is some lifting at that grid point; there is no activation threshold defined for DDL. There is no inherent time/space variation or randomness in this function.

[17] The relationship between the GCM DDL and the model variables upon which it depends are illustrated in Figure 2. These output are taken from a specific grid point in the model at a specific time (lat, lon, season), but are representative of the behavior of the DDL scheme generally within the model. The ground temperature (Figure 2a) provides a direct drive for the sensible heat flux between the surface and the atmosphere, F_{heat} (Figure 2b). As such, there is a clear diurnal cycle of sensible heat flux that is in phase with that of the surface temperature. The η function (Figure 2c) is related to the ground temperature through the convective boundary layer depth (Figure 2d), which has a similar shape to the diurnal cycle of surf ace temperature, but offset by a few hours to later local times (since air temperatures lag the surface temperature). The combination of the sensible heat flux and the η function result in a shift in peak dust devil activity, and hence dust devil lifting in this parameterization, to the early afternoon. This phase shift is in keeping with (results directly from) the predictions of the thermodynamic theory [*Renno et al.*, 1998]. Clearing of dust from the atmosphere is accomplished in the model by gravitational sedimentation. The settling associated with the particle sizes used in this study have been shown to allow the atmosphere to relax back from prescribed dust storms in a realistic manner [see *Wilson and Richardson*, 1999].

[18] The spatial relationship between the net dust injection, dust fallout, and ground temperature (and through intermediary variables) is shown in Figure 3, which presents output from the model at $L_s = 259°$ (where L_s is the seasonal indicator on Mars, measured in degrees from 0° at northern spring equinox). Aside from dictating the pattern of insolation, the season is not important, and the spatial relationships illustrated here hold generally in the model. Surface temperature very strongly controls instantaneous net dust injection (Figure 3a), as one would expect and indicated in Figure 2. Ground temperatures and lifting peak near the subsolar latitude and near noon, with the injection delayed

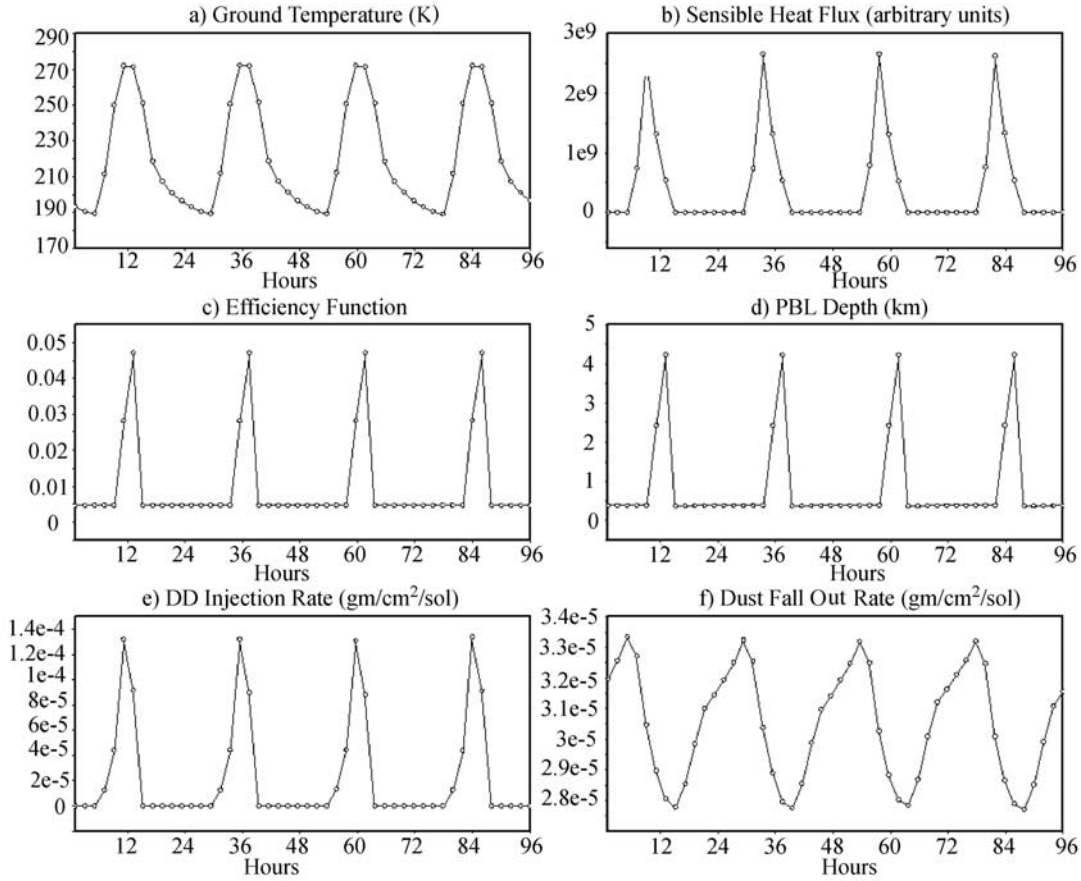

Figure 2. The relationship between predicted dust devil lifting (DDL) rates and various model variables as a function of local time for a point at 0° longitude and 0° latitude for $L_s = 259°$. (a) Solar heating of the surface and subsequent convective motions to shed this heat provide the primary drive for dust devil activity. (b) The sensible heat flux peaks earlier than the ground temperature peak (i.e., in the morning). At this time of day there is greatest contrast between the surface and atmospheric temperatures and consequently the strongest convective drive. (c and d) The thermodynamic theory of dust devils [*Renno et al.*, 1998] suggests a strong dependence upon an "efficiency function" that is itself dependent upon the depth of the planetary boundary layer (PBL). The PBL depth peaks later than the ground temperature maximum (in the afternoon) as it takes time for the PBL to entrain successively higher portions of the free atmosphere. (e) The resulting dust devil injection is a convolution of the sensible heat flux and the PBL depth. (f) The net effect of dust devils can be determined only when the dust fallout rate is also considered. While the fallout is about an order of magnitude lower, the fallout never falls below 80% of its maximum value (at this location), providing a very steady sink. The instantaneous spatial pattern, shown in Figure 3, is therefore much smoother than that of injection.

slightly with respect to ground temperatures. The spatial pattern of convective PBL height is illustrated in Figure 3b. This is similar to plots for other Mars GCMs [e.g., *Haberle et al.*, 1993]. The PBL parameterization in the GCM does not make an explicit prediction of the PBL height, so this value must be calculated. This is done on each time step and for each grid point by deriving the potential temperature for each layer in each model atmospheric column (i.e., at all levels above each grid point) for the predicted air temperatures prior to convective adjustment. Working upward from the surface, when a layer is found whose potential temperature exceeds that of the near surface layer, the pressure of the interface between this higher potential temperature layer and the one below it is recorded as the local PBL top pressure. PBL geometric height is easily recovered by upward hydrostatic integration.

[19] The sensible heat flux (Figure 3c) and η function (Figure 3d) patterns follow those of the ground temperature and PBL depth, much as would be expected from Figure 1. The deviations from a smooth spatial pattern, with values monotonically falling with increasing latitudinal and longitudinal distance from the subsolar point reflect surface variations in the thermal inertia and albedo of the surface via their influence upon ground temperature. In addition, the sensible heat flux pattern is influenced by the circulation through the surface wind stress. These functions combine to yield the net DDL, illustrated in Figure 3e. This figure provides a map of the model-predicted dust devil activity

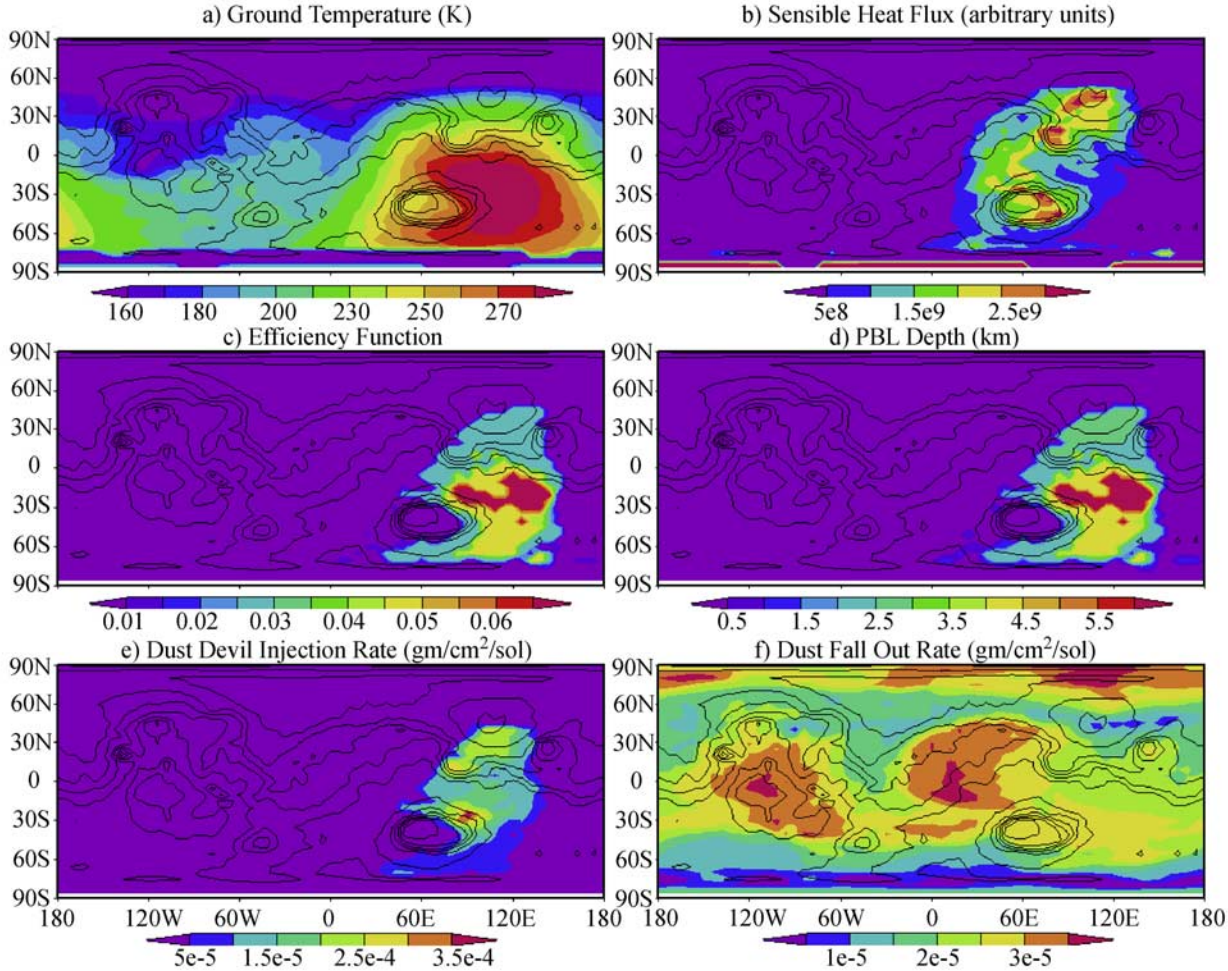

Figure 3. A single time step from the sequence shown in Figure 2, but for all locations on the planet, showing the spatial relationships between the variables.

and provides a gauge of the spatial variation in the relative activity (number per unit area, mean size, etc.) of dust devils. Figure 3f shows the spatial pattern of dust fallout. This is a much smoother function, as the fallout continues whenever dust remains in the atmosphere. In a steady state wherein some dust remains suspended in the atmosphere, the fallout cannot compete effectively with the rate of dust injection where it is highest. As such, the instantaneous injection function (Figure 3e) strongly resembles the pattern of net instantaneous injection (injection minus fallout, Figure 3a).

3.2. Stress Lifting Parameterization

[20] Dust lifting owing to the stress applied to the surface by the drag of model-resolved winds, or stress lifting (SL) for short, is implemented in the GCM in addition to DDL. The scheme assumes that a direct relationship can be drawn between the wind stress and dust emission, as has been observed on the Earth [*Shao*, 2001]. For Mars, this would appear to involve a leap of faith, were it not for images of dust plumes and storms apparently resulting from high wind stresses: Wind tunnel experiments under Mars-like conditions of pressure and temperature, suggest that very high (unrealistic) wind stresses, and hence winds would be needed to directly loft the micron and submicron-sized dust particles found in the Martian atmosphere [*Greeley et al.*, 1992]. Instead, it has become accepted that the wind induces sand-sized particles ($\sim$100 μm) into motion, "saltation," which then impact into dust deposits, causing these dust particles to be launched into the atmosphere. The stress threshold required for sand-sized particle motion is lower than that for dust for reasonable estimates of interparticle cohesion (if there were no electrostatic or other physical cohesion of particles, there would be a continuous easing of the stress threshold for lifting as particle size decreased). As such, while we will talk about the stress threshold for dust injection from this point onward, what we are really talking about is the threshold for saltation of sand-sized particles that then are assumed to inject dust. It should be noted that this conceptual framework requires sand-sized particles (sand or clods of dust) to be present at all locations on the surface, which is of some concern. More generally, the microphysics of dust mobilization is not well understood beyond the general observation from orbit [*Briggs et al.*, 1979; *Cantor et al.*, 2001] and from the ground [*Moore*, 1985] that high winds seem to cause dust injection. If this is true, and by analogy with the Earth, it is likely that wind stresses are the important factor. In any case, we use functions for the SL that have a strong dependence of lifting on wind stress, as would be expected from a wide

variety of wind related lifting mechanisms, be it via saltation or direct lifting.

[21] The parameterization generally used in this study defines the dust injection flux F_{SL} as follows:

$$F_{SL} = R_{SL} \times f(U_{drag}), \quad u > u_{thresh};$$

$$F_{SL} = 0, \; u < u_{thresh},$$

where R_{SL} is a multiplicative rate parameter, ρ is the air density, U_{drag} is the frictional velocity, and where $f(U_{drag})$ can be a simple function of the wind velocity, u, boundary layer eddy diffusivity, and the threshold wind speed, u_{thresh}. SL is threshold dependent; there is lifting only when the wind stress τ ($\tau = \rho U_{drag}^2$) is greater than τ_{SL}, the threshold wind stress corresponding to u_{thresh}. There is no dust lifting when the wind stress is below τ_{SL}. The threshold stress can be taken from wind tunnel experiments [see *Greeley et al.*, 1992]. However, due to concerns over the ability of any numerical atmospheric model to accurately predict the absolute values of surface stress, the possibility that wind tunnel experiments miss some important physics (such as electrostatic effects), and the applicability of local thresholds to the average wind over modeled spatial scales of hundreds of kilometers, we believe it more prudent to use the threshold as a free parameter. Thus the activation threshold wind stress, τ_{SL}, and the multiplicative injection rate factor R_{SL}, yield two free parameters associated with our dust SL scheme.

[22] A variety of functional forms for $f(U_{drag})$ have been developed on the basis of wind tunnel experiments and terrestrial field campaigns [see, e.g., *Shao*, 2001]. Many of these forms show a roughly cubic dependence upon the drag velocity, i.e., $f(U_{drag}) \propto U_{drag}^3$. In the majority of the simulations described in this paper and its companion, a form of roughly this kind is employed (Figure 4a).

[23] A more complex form for $f(U_{drag})$ is described by *Newman et al.* [2002a], which is itself derived from a combination of the formations given by *White* [1979] and *Seguro and Lambert* [2000]. In this formulation,

$$f(U_{drag}) = \int_{U_{dragthresh}}^{\infty} V_N \times w(U_{drag}) dU_{drag},$$

$$V_N = 2.61 \frac{\rho}{g} (U_{drag})^3 \left(1 - \frac{U_{dragthresh}}{U_{drag}}\right) \left(1 + \frac{U_{dragthresh}}{U_{drag}}\right)^2,$$

where V_N is the vertical flux of particles lifted into suspension [*White*, 1979], $U_{dragthresh}$ is the frictional threshold velocity corresponding to the threshold stress, τ_{SL}, and $w(U_{drag})$ is the Weibull distribution [*Seguro and Lambert*, 2000].

[24] The Weibull distribution provides a means of statistically accounting for "gustiness" in the wind by allowing some lifting at wind stresses below the threshold. Use of the Weibull distribution in this way makes $f(U_{drag})$ a continuous function of U_{drag}, even though a threshold stress is specified. When this scheme is implemented, F_{SL} is not set to zero when $\tau < \tau_{SL}$ and some lifting occurs for all values of wind, although the amount falls rapidly for stresses below threshold. The Weibull distribution is given by

$$w(U_{drag}) = (\kappa/c)(U_{drag}/c)^{\kappa-1} \exp[-(U_{drag}/c)^{\kappa}],$$

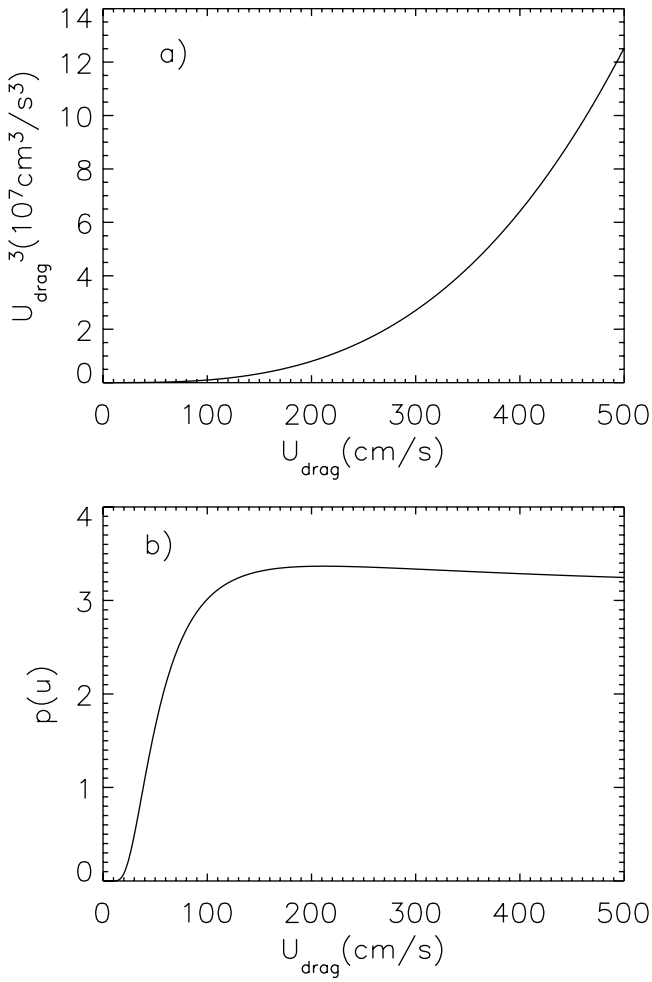

Figure 4. (a) The stress lifting scheme is based on a formulation that relates the dust injection rate to the cube of the frictional velocity (U_{drag}^3). This formulation is used, with some variation, in numerous schemes for terrestrial application [*Shao*, 2001]. (b) In order to capture the statistical effects of gusts, *Newman et al.* [2002a] used a function that does not fall to zero at the threshold frictional velocity for lifting (see text for details). However, this functional form yields a very sharp drop in efficiency below the threshold (150 cm s^{-1} in this example), which is compounded by the cubic dependence on drag velocity. Above the threshold, the function plateaus and does not modify the lifting rate. Due to the simplicity of a scheme with no lifting below threshold and cubic lifting above, we chose not to employ a "gustiness" parameterization.

where c is a scale speed (set equal to the drag velocity output every time step) and κ is a dimensionless shape parameter (low κ values represent high gustiness). Using a value of $\kappa = 1$ [*Lorenz et al.*, 1996] we get the following expression for $f(U_{drag})$:

$$f(U_{drag}) = k \times \rho \times U_{drag}^3 \times p(u),$$

where $p(u) = (2u^2 + 4u + 3)/\exp(u)$, $u = U_{dragthresh}/U_{drag}$, and k is a constant. This relation provides a function that is

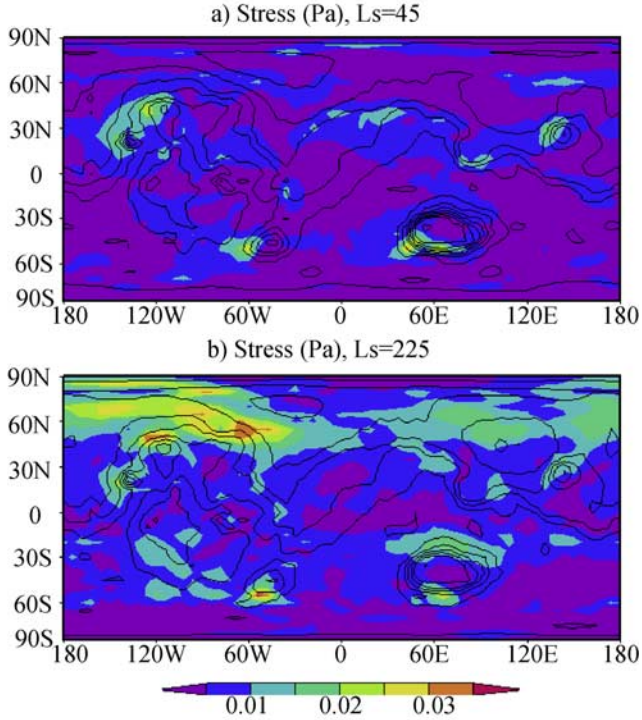

Figure 5. Diurnal-mean surface stresses for (a) L_s = 45 and (b) L_s = 225. The topography is contoured in black. The results are for the no-threshold SL case.

zero for Udrag = 0, and grows, dominated by the exponential term, to a value at $u = U_{dragthresh}/U_{drag} = 1$, at which the function essentially plateaus for $U_{drag} > U_{dragthresh}$ (Figure 4b). The prediction of some lifting for $U_{drag} < U_{dragthesh}$ with this function is an attempt to capture lifting due to gusts at scales not resolved by the model. The value of κ chosen determines how sharply lifting declines as the U_{drag} decreases below the threshold.

[25] In either case, for values of wind stress above the threshold, the lifting rate is $\propto U^3_{drag}$ and the only difference is the sharpness of the stress threshold cut off for lifting for $U_{drag} < U_{dragthesh}$. Partly because a very much simpler interpretation of the results emerge if the threshold is sharp, partly because it seems useful to employ a physically simple parameterization for a system that is poorly understood, and partly because the observations in hand [e.g., *Moore*, 1985, *Zurek et al.*, 1992] do not appear to readily support the widespread, low-rate dust injection that the continuous scheme generates, we chose to use the simple, threshold-dependent, U^3_{drag} scheme.

[26] A consequence of the threshold-dependent scheme is that dust is only lifted where the wind stress exceeds a preset value. Some idea of the fraction of the surface from which dust is being lifted at any moment in the model can be gauged by examining snapshots of the surface wind stress. Figure 5 shows such stress distributions at the central meridian for $L_s = 45°$ (mid northern spring) and $L_s = 225°$ (mid southern spring). From this figure, it is easy to appreciate that the choice of stress threshold effectively is a choice of what fraction of the area of the surface that one wants the model to lift dust from at any given time. Specific regions of the planet tend to be associated with higher stress, such as along the eastern side of the Tharsis plateau, in and around the Hellas basin, along the seasonal ice cap edge, and along the convergence zone of the Hadley circulation. Lesser dust lifting activity occurs elsewhere in the domain. As the threshold is increased, the locations of dust lifting become increasingly tightly constrained to the major high stress zones.

4. Fitting the Annual Cycles of Air Temperature and Dust

[27] The combined GCM dust injection parameterization has three free parameters that can be set to unique, globally and spatially fixed values for a given simulation. All simulations were run for more than one year to check for variability and to allow assessment of the full annual cycle. The seasonal cycle of globally averaged air temperatures was used as our primary metric for checking the quality of simulations, as it is the thermal state that is most important for determining the dynamic response of the atmosphere. The procedure for evolving the free parameters toward values that yielded a realistic climate simulation involved checking the annual cycle output, assessing whether the simulation was too cool or too warm, and then adjusting the injection to higher or lower values, accordingly. For clarity and in order to develop some intuition about how the two injection schemes influence the climate simulation, we initially examined the convective and wind stress lifting schemes separately, before proceeding to look at combined injection simulations. For simulations that met the minimum requirement of fitting the global-average temperature trend, the zonal and height variations of temperature were then examined for more detailed insight (section 5).

[28] In this study, we present both dust injection scheme rate parameters in arbitrary units. The main reason for this is that we have found that a given set of parameter values will not produce the same climate when model resolution is changed. We believe that these parameters would not yield the same climate if used in a different GCM (variations in boundary layer scheme will likely also have a significant impact). As such, we wish to emphasize the importance of the tuning process and approach, rather than the specific values of the rate parameters. In this light, appropriate reproduction of our results (or not) depends upon using our tuning technique, not on using our rate coefficient values. One obvious concern regarding this approach that reader ought to bear in mind is whether our injection rates yield a characteristic lifetime of dust in the atmosphere that is consistent with observations. We examine the lifetime explicitly at the end of this section, finding lifetimes that are consistent with lifetime observations derived in the decay phases of dust storms.

[29] The climatology of midlevel air temperatures is taken from the multiyear, multispacecraft T15 record compiled by *Liu et al.* [2003] and introduced in section 2 and Figure 1. As a curve, the air temperature data provide a very compact and easy-to-digest metric against which to test the model. In all cases, ''synthetic'' T15 data are generated from the model by application of the IRTM 15-μm channel weighting function to individual pressure-temperature profiles. Such

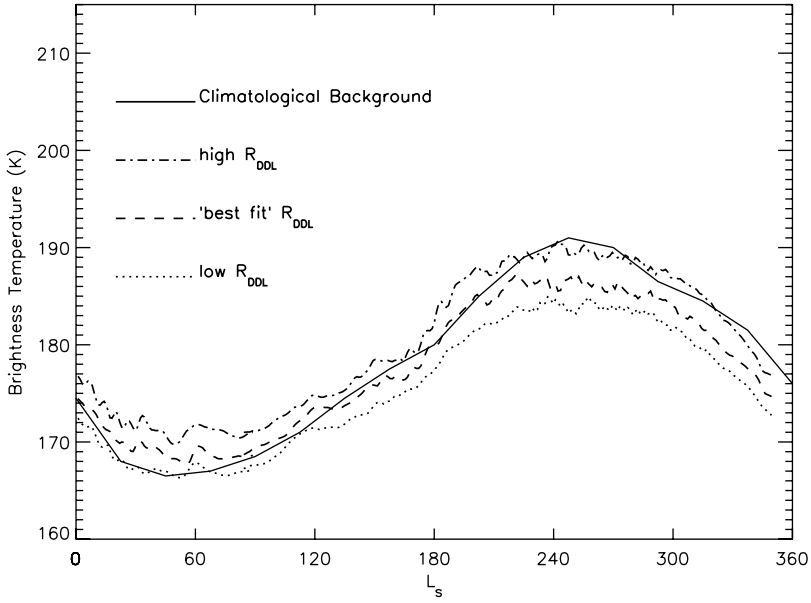

Figure 6. Atmospheric temperatures predicted by the model and observed. Model results are shown for different values of the dust devil lifting scheme rate parameter, R_{DDL}. The climatological background (Figure 1) is plotted for reference. A very good fit to the air temperature curve through northern spring and early northern summer is obtained with relatively low rates. Somewhat increased values are needed to fit the late northern summer temperatures, though the observed temperatures in this seasonal range may be influenced by increasing dust storm activity. In southern spring and summer the determination of the "background" climatology is extremely difficult, and there is likely always some influence of dust storms.

model output have been shown by *Wilson and Richardson* [2000] and *Richardson and Wilson* [2002].

4.1. Dust Devil Source

[30] The dust devil lifting (DDL) parameterization has a single tuning parameter, which is the injection rate coefficient discussed in section 3.1. As such, the fitting process is very straight forward. Without any atmospheric dust, the model produces air temperatures that are about 15K cooler than observed (Figure 1). In order to increase these temperatures, dust is needed in the atmosphere to absorb solar radiation. Since the amount of dust injected into the atmosphere is controlled by the rate parameter, it can be adjusted until a good fit is obtained at some point in the year. We place most emphasis on the northern late spring and early summer ($L_s \cong 20°-140°$), as this is the period for which the real atmosphere has a high degree of repeatability [*Richardson*, 1998; *Liu et al.*, 2003] as it is least affected by large dust storms.

[31] Figure 6 shows several curves corresponding to different dust injection rate parameters (R_{DDL}) in section 3.1. In each case, the shape is similar, with the main difference being translation of the curve to higher (lower) temperatures with increased (decreased) injection rate. As there is no physical basis for allowing the injection value to change with location or season, we use a single value of R_{DDL} at all grid points and at all times in any given simulation. Each simulation is begun from an initially spun-up state, with the simulation being run for sufficient time that there is no sensitivity to dynamical initial conditions. The pressure cycle is tuned by modifying the total amount of available CO_2, which partitions itself between seasonal ice and atmospheric gas. As a result of starting from a steady state condition, startup transients for each simulation set are minimized. The simulations are allowed to come to steady state by running the model for one year before analysis of any given simulation (the simulations were found to come into steady state in less than 100 days). Note that the particular thermal state of the restart file does not influence the final climate simulation, as has been gauged by running the model with a fixed set of injection parameters from "restart" files with different initial states.

[32] Since the DDL scheme has no time-varying parameters, we have no control over the "shape" of the modeled annual air temperature cycle (by "shape" we mean the curve in the air temperature data as a function of season). The shape is therefore an intrinsic character of the DDL scheme and its response to forcing. It has been shown before that very simple schemes designed to mimic convective processes (using a very a simple function of surface-atmosphere temperature contrast) can produce a seasonal cycle shape that is relatively good agreement with observations [*Richardson and Wilson*, 2002]. The details of the shape are interesting and somewhat more complicated than they may superficially appear; however, their discussion is deferred to a later paper focusing on detailed interpretation of the observed seasonal cycle on Mars. Suffice it to say that ability to fit the shape is not a controllable factor and, in consequence, the fact that the DDL scheme can fit the curve reasonably well (Figure 6) is an important piece of evidence suggesting that either DDL itself or the pattern of forcing driving it are of fundamental importance in generating the

annual cycle of air temperatures via the dust loading. In contrast, constant opacity simulations yield quite different curves, with dual temperature maxima in southern spring and summer. It should be noted that no matter how high the R_{DDL} parameter was set, variable global dust storms could not be generated (we take the firm view that a simulation with interannually repeatable high dust loading in both summers is not generating global dust storms, but instead is simply generating a climate with unrealistically high background dustiness). Further, as the R_{DDL} value was increased above the "realistic" range shown in Figure 6, the shape of the northern summer temperature trend worsened progressively.

[33] As shown in Figure 6, it is possible to find values of R_{DDL} that provide a good fit to the climatology curve, to the level of precision of the climatology (the dust devil fits do show a slight deviation in shape in northern spring, where they can be up to 3–5K too warm). The particular R_{DDL} value that gives the fit (in fact there is a range of values within which it is difficult to pick due to uncertainty in the data and noise in a given year's simulation) is provided in the figure caption (but see the note at the beginning of section 4 for our advice on use of this value).

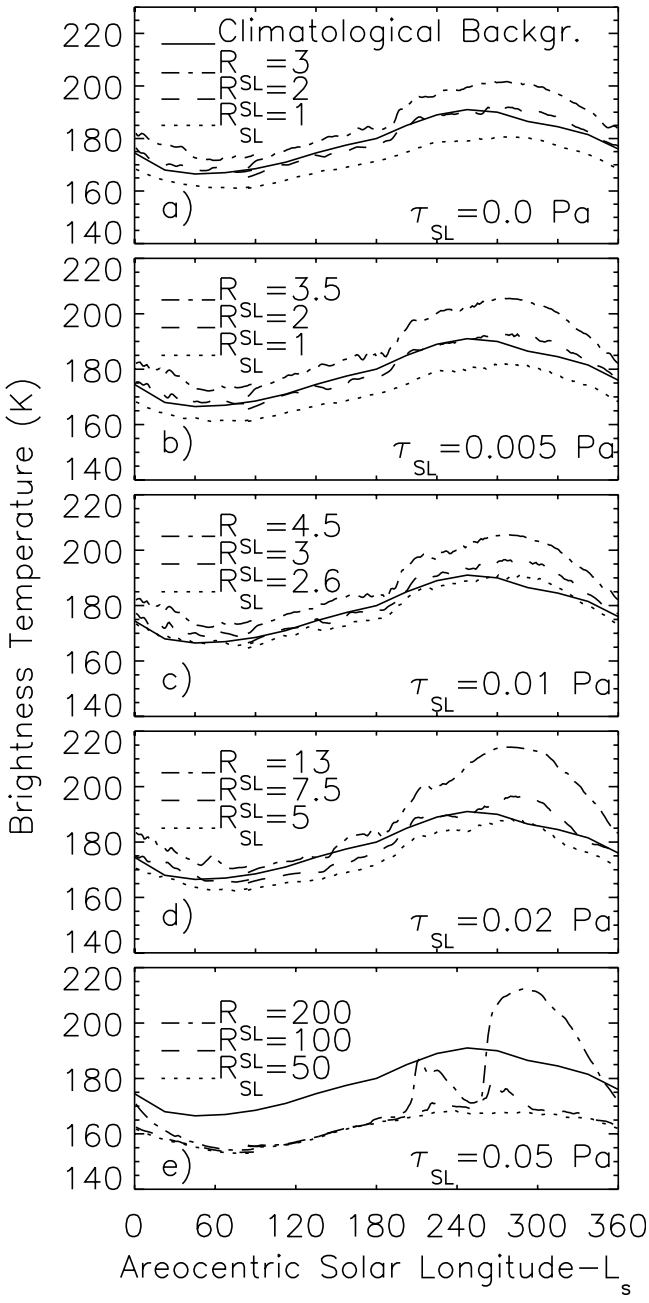

4.2. Model-Resolved Wind Stress Source

[34] It is possible that dust lifted by winds associated with mesoscale and synoptic-scale systems (>10 km), rather than microscale convective systems (<10 km) provides the continual dust injection that supplies the background haze. An analysis of dust devil streaks in Hellas has recently been used to argue that dust devils indeed cannot supply this haze, and that injection by larger systems is necessary [*Balme et al.*, 2003]; however, a study of dust devils at the Mars Pathfinder site suggest just the opposite [*Ferri et al.*, 2003]. These analyses are discussed further in section 6. In any case, clear motivation exists to see whether wind stress lifting alone can maintain the background dust haze, and if it can do so within the constraints of dust lifting observations from imagers, and while simultaneously generating dust storms. Unlike the DDL experiments, the stress lifting (SL) experiments require investigation of two parameters: the rate and threshold parameters. As such, our procedure has been to find the set of combined rate and threshold parameters that yield a reasonable seasonal temperature trend.

[35] Figure 7 shows results from 15 different GCM multiannual simulations exploring combinations of stress threshold and rate parameters. The results show that there exist combinations of the two parameters that yield seasonal temperature curves that fit the observed climatology as well as the best fit DDL case. For each stress threshold, the trend with increasing injection rate is simply to translate the seasonal curve to high-temperature values, just as was found for the DDL-only scheme. The quality of the shape fit for the SL-only scheme is found to be best for the no-threshold case, worsening very slightly with increasing threshold up to a value of roughly 0.02 Pa (for our model).

Figure 7. The seasonal cycles of simulated air temperatures compared to the climatology for various values of stress threshold and injection rate parameter. The threshold is shown in the bottom right of each panel (τ = 0, 0.005, 0.01, 0.02, and 0.05 Pa for Figures 7a–7e). The rates in each case but Figure 7e bound the observed temperatures. The best fit to the northern late spring and early summer temperatures is provided by the no-threshold case, with the fit worsening as the threshold increases. The injection rate values can meaningfully be compared between figures (i.e., the highest injection rate multiplier shown in Figure 7d is thirteen times greater than that of the lowest rate multiplier in Figure 7a). For Figure 7e the threshold is sufficiently high that essentially no lifting occurs in northern spring and summer, despite the use of injection rate two orders of magnitude higher than in Figures 7a–7c. Note instead that Figure 7e exhibits air temperature spikes associated with dust storms in southern spring and summer, which are not produced in the other cases.

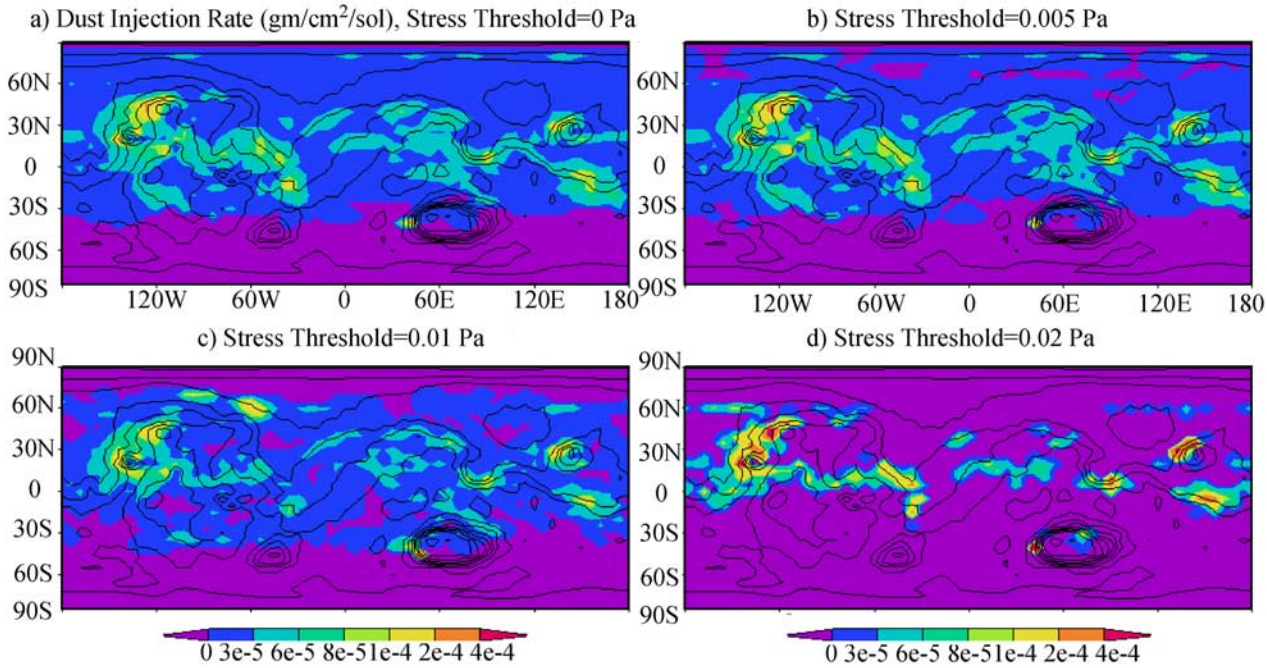

Figure 8. The spatial distribution of dust lifting predicted by the model for a single two-sol period, at northern summer solstice, for the middle injection rate cases shown in Figures 7a–7d. Very widespread dust injection is required by the model; this pattern compares reasonably well with that for convective lifting. Relatively steady and widespread predicted lifting provides the opportunity to test the importance of wind stress lifting. The local dust storm catalog developed by *Cantor et al.* [2001] shows local storm activity to be much too concentrated and limited to too few occurrences to fulfill the role required by the model.

By the time a threshold of 0.05 Pa is reached, no amount of dust injection will allow the model to fit the observations. In this case, the threshold is too high for the surface winds to activate dust lifting. The temperature curves for the periods between $L_s = 60°$ and $L_s = 180°$ for this threshold correspond to that of a completely dust free atmosphere.

[36] The effect of increasing the threshold is to decrease the fraction of the planet's surface area that can participate in dust injection. Inhomogeneity of topography, other surface properties, and the large-scale circulation generate spatial variations in the maximum obtained stresses; as the stress threshold is increased, this threshold exceeds the maximum obtained values for certain regions, and they are no longer active dust sources. This trend can be seen in Figure 8, which provides a snapshot of dust injection (not net injection) for the best fit curve for each of the thresholds shown in Figure 7. While the spatial pattern of peak lifting remains constant (for all but the 0.05 Pa threshold case), the area contributing dust decreases monotonically. This trend of less of the surface contributing to dust injection as stress threshold increases (and hence greater sensitivity to small variations in stress behavior at these few locations) is an important part of the mechanism of interannual dust storm variability to be discussed in the companion paper.

[37] Figure 7e also provides support to the idea that global storms cannot be responsible for maintenance of the background dust on Mars. The highest dust injection rate simulation in this set generated a significant dust storm in the early southern summer, which exhibited dust and temperature decay rates that are consistent with observations of the decay of the 1971 and 1977b storms. However, by $L_s = 60°$ in the following year, temperatures had returned to the "clear atmosphere" level, consistent with the other simulations for this threshold. To the extent that the model provides a good simulation of the Martian atmosphere, it confirms the idea that the Martian atmosphere does not have system "memory" that extends over more than half of the annual cycle.

4.3. Summary of Dust Source Results

[38] One important question regarding the DDL and SL simulations described above centers on the injection parameters yielding realistic injection rates. Realistic in this case means that the mass of dust moved between the surface and atmosphere is consistent with the mass of dust suspended in the atmosphere. It also involves issues of control; if the amount of dust cycling daily between the surface and atmosphere is vastly greater than the mass in the atmosphere, it suggests a less direct control of atmospheric opacity by the injection scheme than by the boundary layer mixing scheme, for example. Our use of arbitrary injection coefficients makes determining this realism difficult without further discussion. In this light, Figure 9 shows the trend in global-mean dust injection and global mean dust fallout for the best fit DDL-only, SL-only, and combined DDL and SL "best fit" simulation (for years with and without a global dust storm). These figures show the phase delay between injection and fallout, and particularly for the dust storm case (Figure 9c), the smoothing of the storm fallout signal compared to the sharp injection signal. More importantly,

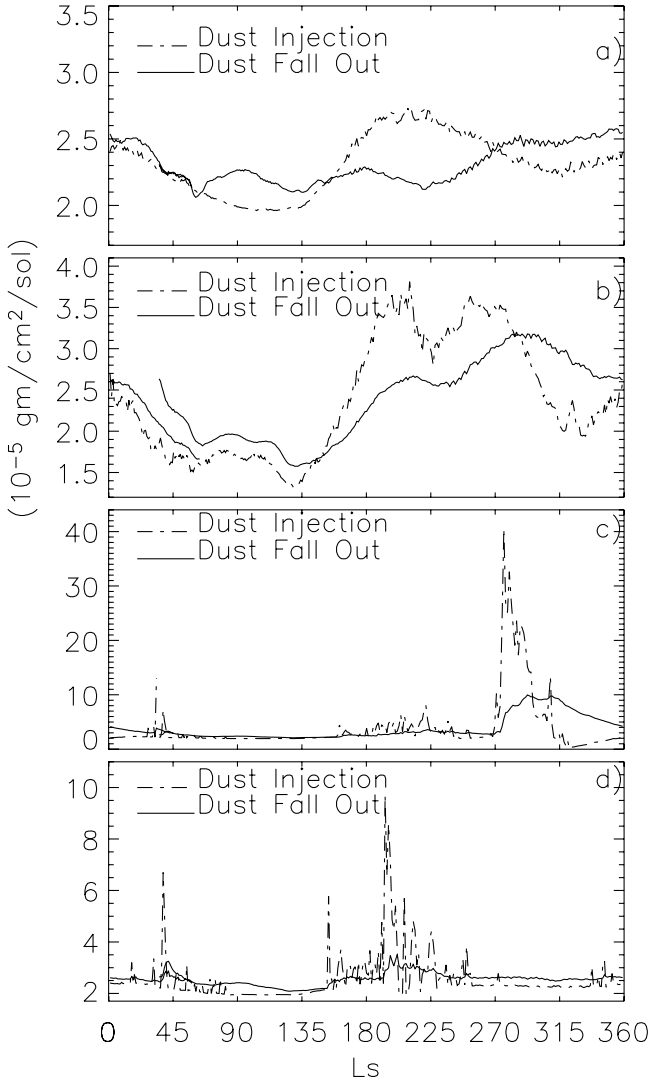

Figure 9. The globally averaged rates of injection and settling of dust indicate an atmospheric exponential lifetime for dust of a few tens of days. The seasonal trends in dust injection and settling show perturbations in settling lagging perturbations in injection. The cases shown are (a) convective lifting only, (b) no-threshold stress lifting only, and years from the combined "best fit" simulations for years (c) with and (d) without a global dust storm. For the dust storm it is interesting to note the smoothing of the settling pulse relative to the injection pulse and the abnormal suppression of dust injection in the wake of the global storm. During this storm decay period, the high dust opacities cause the model surface-atmosphere temperature contrasts to become much smaller than usual, producing a strong negative feedback on dust lifting. The phase lag is of course due to the fact that settling is proportional to dust loading and so the source must have time to build a dust loading before settling can build up. The smoothing represents the different influences on injection timescales (dynamical mixing) and settling (gravitational sedimentation).

combined with knowledge of the annual-mean atmospheric dust mass, the annual mean injection can be used to derive the atmospheric lifetime of dust. Using an annual injection rate of 2.35×10^{-5} g cm^{-2} sol^{-1} and an atmospheric dust mass of 2.9×10^{-4} g cm^{-2} (both from the DDL simulation), we obtain a lifetime of roughly 12 sols for an average dust grain. Other simulations yield lifetimes in the low tens of sols (10–30 sols). These mean lifetimes are consistent with injection control of the dust abundance and with the injection rates being realistic in comparison with fallout rates determined following large dust storms; our rate parameter values are not masking dramatically unrealistic injection rates.

[39] Comparison of Figures 9c and 9d, showing annual cycles from the same simulation, but for years with and without a global dust storm, shows an interesting feedback on DDL lifting. In the wake of the global storm (at L_s = 270° in Figure 9c), the injection rates fall to the lowest level observed at any time during the simulation. Comparing the values at L_s = 325° in the two years, following the storm the injection is about 5×10^{-6} g cm^{-2} sol^{-1}, compared to the non-dust-storm year value of about 2.25×10^{-5} g cm^{-2} sol^{-1}. In this case, the greater stability of the atmosphere (and smaller daytime surface-atmosphere temperature contrasts) corresponding to higher atmospheric temperatures induced by dust heating, yields a significant reduction in convective activity and DDL injection. Examples of this kind of negative feedback on the DDL scheme were also pointed out by *Newman et al.* [2002a]. Feedbacks within the atmosphere associated with global dust storms are discussed by B04.

[40] The low-threshold SL simulations yield good fits to the seasonal cycle of atmospheric temperatures. However, a given set of SL parameters cannot simultaneously yield both a good cycle of background temperatures and spontaneous and variable global dust storms (discussion of which is provided by B04). This suggests either that SL is not responsible for maintenance of the background haze or that the real system corresponds to multiple SL values being used simultaneously. For example, if injection were to be the sum of an SL scheme with low threshold and low rate, and another with high threshold and high rate, it is possible to yield a simulation with a good seasonal fit and with spontaneous and variable global dust storms. How reasonable is this? One can imagine that within the area of a given GCM grid box, substantial variability exists such that certain subportions of the domain can easily be prompted to inject dust, while others require much higher wind stresses to trigger, much as is the case on scales resolved by the model. However, the injection rates employed when these two stress thresholds are exceeded are vastly different (orders of magnitude differences are needed to simultaneously yield the right climatology and dust storms). It is far less clear how physically defensible these differences are (though one possibility is downslope wind storm acceleration on the lee of unresolved topography [*Magalhaes and Young*, 1995]).

[41] The spatial pattern of no-threshold SL lifting is similar to that of DDL during northern spring and early summer (see section 5.2 and figure therein). This similarity in spatial pattern likely explains the similarity in the ability of these two schemes to fit the background haze cycle. The

dominant control of this pattern for DDL is clearly associated with the spatial variation of thermal convective vigor, as discussed in section 3.1. That the no-threshold case SL and DDL produce a very similar spatial pattern suggests that a major control on the injection, via the imparted wind stress, is through the variation of the drag parameter associated with variations in the vigor of convective activity during the day. This similarity does not argue for one injection process over the other, but suggests instead that the controlling physical processes might not be as distinct in the two schemes as one might expect at first glance.

[42] Discrimination between DDL and SL roles in the maintenance of background haze most likely can be made on the basis of observations. The DDL scheme predicts widespread and ongoing dust devil activity, and particular seasonal variation of injection. Images of Mars from orbit and from landers show abundant dust devil activity in the form of dust devils and dust devil tracks across the planet [*Metzger et al.*, 1999; *Malin and Edgett*, 2001; *Cantor et al.*, 2002; *Fisher et al.*, 2002; *Balme et al.*, 2003; *Ferri et al.*, 2003]. As shown at the end of section 5.2, the model predictions of dust injection during northern summer agrees remarkably well with the estimates of dust devil lifting from Imager for Mars Pathfinder data analysis [*Ferri et al.*, 2003].

[43] The model also predicts that if low- or no-threshold SL controls the background haze, widespread and continuously ongoing non-dust-devil lifting should be active. Figure 8 shows low-threshold injection averaged over 2 sols, requiring dust lifting within each grid box over a very large fraction of the planet's surface. However, in the exhaustive survey of local dust storms described by *Cantor et al.* [2001], for the period near $L_s = 110°$, on any given day, only two or three storms with areas over 10^3 km^2 were counted over the entire planet. This is a vastly smaller area of dust lifting than that predicted by the no-threshold SL case, and more in keeping with the very much higher threshold SL cases required to generate large storms. Systems smaller than about 100 km^2 cannot be observed in the MOC daily global map images, but are very rarely even seen in the MOC narrow angle images (at 1–10 m resolution), which would seem to be inconsistent with the widespread, regular lifting predicted by the no-threshold SL simulation (the low resolution of the daily global map images also precludes the use of this data to capture the total number of dust devils occurring on a given day below the spacecraft track).

[44] Other types of dust lifting, apart from dust devils and local storms are possible. Dust streaks are evident on the surface associated with craters and other forms of sharp topography [*Thomas et al.*, 1981, 1984], and the high stresses in the lee of these objects might be important (obviously it is only dark, erosional wind streaks that are of interest as potential sources of dust). One factor arguing against the role of lee stresses is frequency of activity: fitting of wind directions to observed streaks suggest that they form rapidly by eroding nonequilibrium dust deposits (such as those deposited following a large dust storm) at specific times of day when the stresses are highest [*Fenton and Richardson*, 2001; *Thomas et al.*, 2003]. However, lifting can only be sustained until these very limited areas are depleted (yielding the dark streak). We are therefore dubious of the role of such lifting, but this is a bias that requires a focused study before conclusions can be drawn. Finally, it is possible that some microscale lifting process is at work that is below the resolution of orbiting cameras, but is also never seen in lander images. To determine if such "stealth" lifting is ongoing to the degree required by the SL scheme, it may be necessary to measure the net vertical flux of dust on future landers.

[45] In summary, the observed lack of dust motion at the Viking Lander sites except during extreme wind events [*Moore*, 1985], and the only observation of dust lifting at the Pathfinder site being associated with dust devils [*Metzger et al.*, 1999], also argue that nonconvective lifting of dust is rare at most locations on Mars. Local dust storms are insufficiently active, based on comparison with the *Cantor et al.* [2001] catalog. Given the abundant evidence for dust devils across the surface, and the lack of observations of an adequate non-dust-devil lifting mechanism, it seems that the dust devil lifting mechanism is the most plausible. This interpretation is further supported by the ease with which the annual cycle can be fit with a combination of DDL and high-threshold SL, but that a combination of high and low SL is needed if DDL does not dominate the haze maintenance, and that these two SL modes require orders-of-magnitude different injection rate parameters. Plausibility would currently seem to us to strongly support a dominant role for dust devils in the maintenance of the background haze. However, further observational study is needed before this opinion can be established as a fact.

5. Characteristics of the "Best Fit" Model Annual Cycle

[46] Examination of the model seasonal cycles described in section 4 and associated arguments can lead to a paradigm for a "best fit" model climate in which DDL lifting provides control of the seasonal haze cycle and SL control of dust storms. In this way, a "best fit" annual cycle simulation can be found by varying the R_{DDL} until the background seasonal air temperature cycle is fit (with emphasis on northern spring and summer), and then varying the R_{SL} and τ_{SL} values until variable dust storms are generated in southern spring and summer. A very large amount of phase space was examined, as shown in Figure 10. This figure summarizes the dust storm simulations (all using the same DDL parameters), categorizing them on the basis of whether they yielded realistic non-dust-storm climates and the nature of the dust storm activity generated. An area of phase space was found in which spontaneous and interannually (and intra-annually) variable global dust storms were produced in southern spring and summer, and which would relax back to a realistic thermal state after these events. Output from such a "best fit" case is described in this section. The dust storms generated by this simulation are described in some detail by B04.

5.1. Meridional and Vertical Distribution of Air Temperature

[47] For a year without a major dust storm, Figure 11 shows the comparison of the seasonal cycle of meridional midlevel air temperatures with observations (IRTM T15

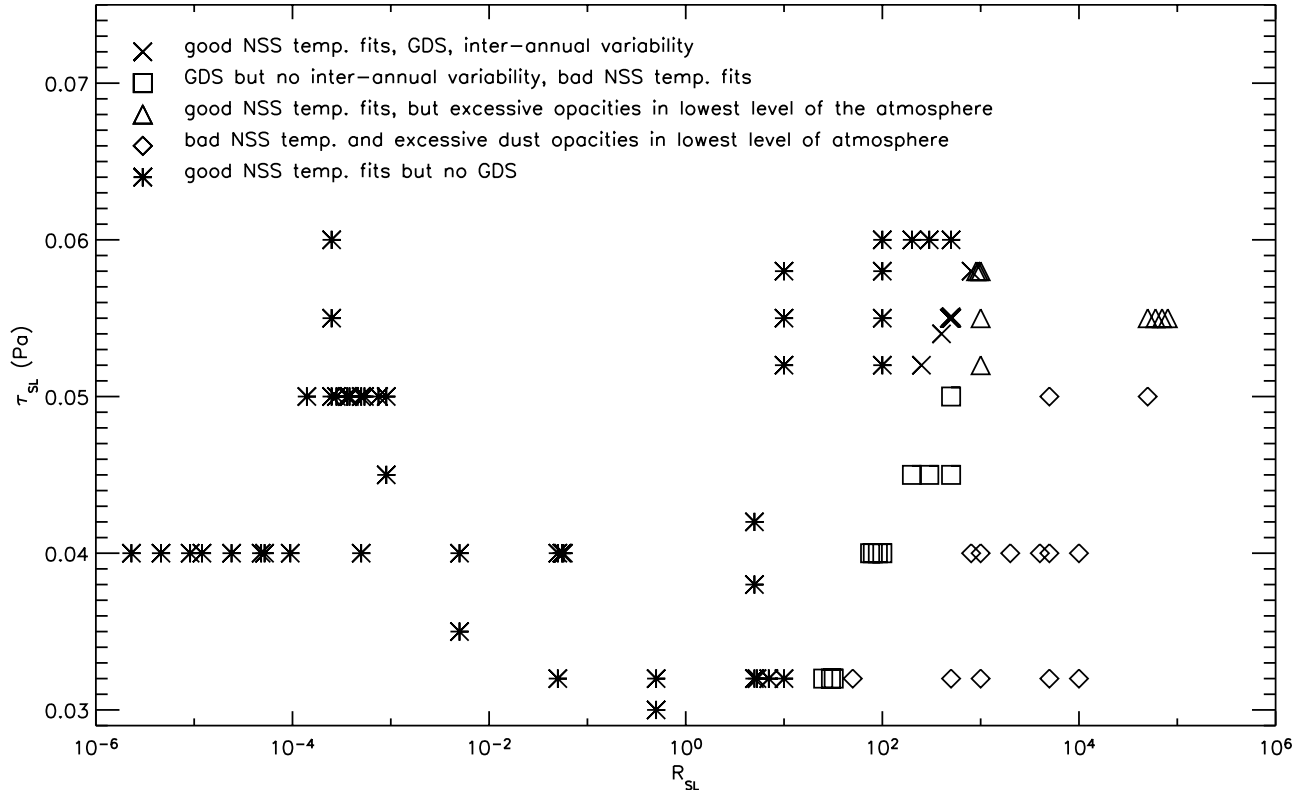

Figure 10. A summary of the wind stress scheme phase space examined for various dust storm behavior. In all cases, the best fit DDL injection parameters were used, and only a single set of wind stress parameters were used in a given simulation. In a specific area of phase space (indicated), spontaneous and variable global dust storms were simulated in southern summer, emerging from and returning to realistic non-dust-storm states in northern spring and summer. Significantly, these simulations exhibited years with and without global storms within the same multiannual simulation. This figure and the study are discussed in greater detail by B04. NSS here refers to Northern Spring and Summer, and GDS refers to Global Dust Storm.

values synthesized from the TES data [*Liu et al.*, 2003]. This comparison indicates that not only have ''global mean'' temperatures been fit, which was the tuning metric, but also the meridional gradients. In particular, the double peak of air temperatures in both midlatitudes, and local minimum in the tropics during summer is an indication of the Hadley circulation. The TES data are an average of day and night spectra from the mapping orbit. In order to provide best comparison, the GCM has been sampled at 2pm and 2am local times to mimic the MGS mapping orbit. Specifically, the observation-by-observation sampling of the model mimics that of the TES sampling of the atmosphere at the same latitudes, longitudes, local times, and seasonal dates (obviously, some interpolation of model output is involved as the GCM generates output for a simple cylindrical grid at 5° by 6° grid spacing, and with an output interval of 2 Martian hours). As such, there are no biases due to the small changes in local time of the MGS orbit, due to gores in the TES latitudinal coverage, or due to asymmetry in the number of day-side versus night-side observations.

[48] The difference between the GCM output and the TES observations (Figure 11c) suggests that the model captures midlevel air temperatures well throughout most of the year. In the tropics and midlatitudes, the individual bin differences are within ±5K, with no discernable spatial pattern, and averaging to much less than 1K. Major exceptions to this consistency in the tropics and midlatitudes occur at roughly $L_s = 200°$ and $L_s = 235°$ when, first the GCM develops a small regional storm not present in the TES first mapping year observations, and then the real atmosphere develops a planet encircling dust storm (while not global, this storm was the largest event of 1999, and began in a most interesting manner [see *Wang et al.*, 2003]), which is not present in the GCM simulation. In very late southern summer, the GCM cools somewhat faster than that of the real atmosphere, ending the year roughly 5K cooler. This is not a consistent, multiannual offset, however. At the beginning of the model year shown, the dust and hence air temperature decay is somewhat slower than the MGS second mapping year data shown. As a result, the simulation is as much as 10K warmer than the observations for the first 30°–40° of L_s of the year. These discrepancies occur during the periods of the year known to be more variable from the observations [*Liu et al.*, 2003]. During the majority of northern spring and summer, the air temperatures are very close, and again within the spread of observed year-to-year variability (which during this season, is mostly due to ''weather'' and instrument noise).

[49] The polar regions show more of a discrepancy than the tropics and midlatitudes. In southern spring and summer, this is mainly due to the action of the 1999 planet-

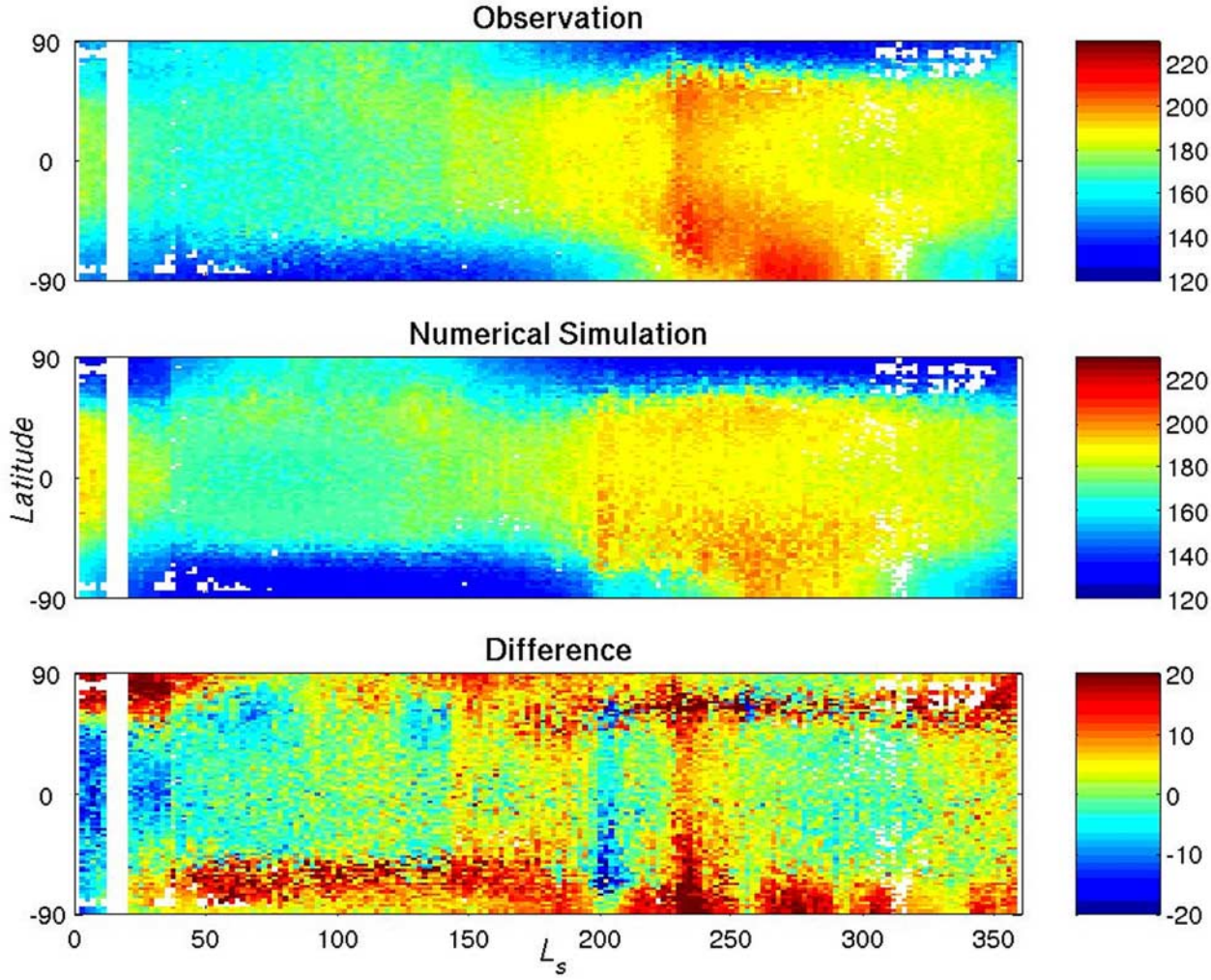

Figure 11. A comparison of zonal-mean 15 μm channel temperatures derived from the MGS TES spectra and from the GCM. The GCM output was sampled using the TES observational pattern to maximize comparability. A full annual cycle is shown for each, along with the difference between the model and data. The results are for a nonglobal dust storm year (the first MGS mapping year from northern summer and rolling around into the second) and from the "best fit" GCM simulation.

encircling storm and a regional southern polar storm. Real atmospheric temperatures are warmer than the model in the high southern latitudes where there is higher dust opacity and solar dust heating, and in the high northern latitudes, in a band near 60°N. This corresponds to stronger Hadley cell downwelling, and a consequent poleward movement (contraction) of the polar vortex wall. Temperatures over the northern winter pole (>70°N) are well simulated. In southern autumn and winter, the GCM predicts southern polar temperatures that are too cold by between 5 and 15K (with the larger discrepancy at the vortex wall, at the latitude of maximum temperature gradient). It would seem that the GCM somewhat over predicts the isolation of the southern polar vortex in southern winter. Over the pole (>85°S), the error is less than 5K. The GCM also substantially underpredicts (15–20K) air temperatures in the decaying northern polar vortex in late northern winter and early northern spring. Again, the GCM seems to be somewhat over predicting vortex isolation (underpredicting meridional heat fluxes). After L_s = 50°, the fit becomes very good all the way to the northern pole. Thus, with the exception of the winter polar vortices, the GCM is able to fit the latitudinal distribution of midlevel air temperatures to better than 5K. This fit includes a good prediction of the seasonally varying polar vortex walls, and the locations of downwelling in the solsticial Hadley circulations (illustrated by the double maxima in the latitudinal temperature gradient in both northern and southern summer [see *Wilson and Richardson*, 2000]). The winter polar area arises due to underprediction of meridional heat transport across the vortex, due to error in prediction of cap-edge dust storms and/or other atmospheric eddies.

[50] Zonal-mean temperatures are compared with TES observations for both solstices and equinoxes in Figures 12–15. In addition, the model dust distribution, stream function, and zonal wind distributions are shown. For northern summer solstice (Figure 12), there is generally good agreement between the observed and simulated

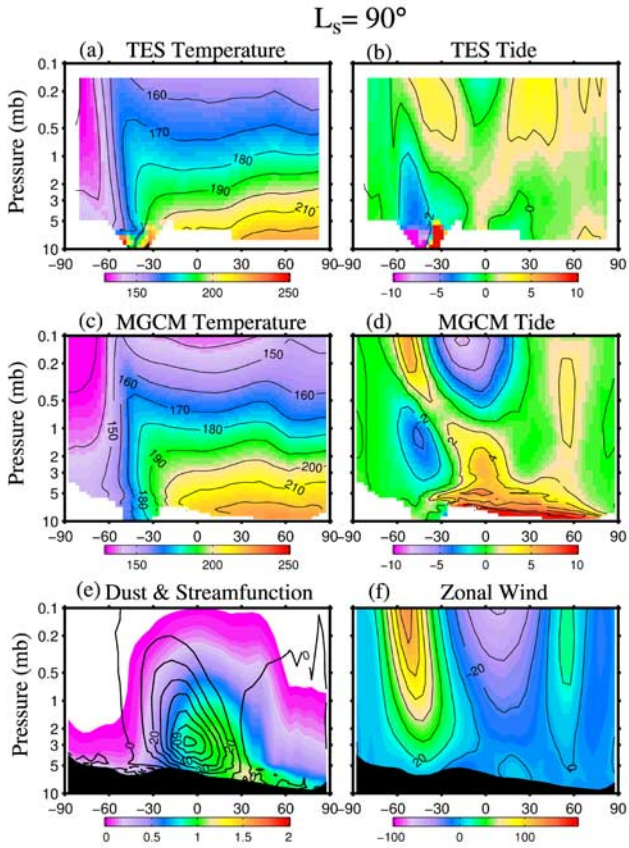

Figure 12. Cross sections of zonally averaged thermal structure for L_s = 90°. (a) Observed TES diurnal-average temperature structure. The diurnal average is defined as 0.5 × (T2pm + T2am). The contour interval is 10 K. (b) The corresponding diurnal difference field (T2pm-T2am). The contour interval is 2 K. (c) Temperature structure simulated by the GCM. (d) The simulated diurnal difference field. Simulated fields have been interpolated to a common pressure grid prior to zonal averaging. (e) The simulated dust distribution (color shading) and mass transport stream function (contours). The aerosol opacity is scaled to show the contribution to column integrated total opacity as if the local contribution were representative of the total column (i.e., the local mass mixing ratio value has been used to calculate the total column opacity, were the total column to be uniformly that mass mixing ratio). Stream function contours are in intervals of 10 by 10^8 kg s^{-1}. Positive (negative) contours are associated with a counterclockwise (clockwise) circulation. (f) Simulated zonal mean zonal velocity. The contour interval is 10 m s^{-1}.

diurnal average temperature fields. The most notable differences are in the tropical lapse rate and the meridional temperature gradient at high latitudes in the summer hemisphere. Below roughly the 1 mb, the highest observed temperatures are in the summer pole region where insolation is greatest at this time of year. By contrast, the simulated temperatures are more meridionally symmetric, with maximum temperatures (on a given pressure surface) at midlatitudes. The temperature differences most likely stem from the lack of dust at high latitudes in the summer hemisphere. The simulations fail to reproduce the observed dust storm activity along the margin of the retreating CO_2 ice cap with the observed vigor (though some cap edge storms are generated; see section 5.3). There is a tropical temperature bias such that the simulated low level temperatures are slightly too warm while above 0.5 mb the simulated temperature profile becomes increasingly cold. This bias may reflect deficiencies in the simulated dust distribution, deficiencies in the temperature retrieval, or the absence of additional radiative agents, such as water ice clouds. The simulation includes dust presenting 0.6 and 2.5 μm particles. It is possible that a different size distribution would lead to a deeper distribution of dust, and possibly greater radiative forcing at higher altitudes. More detailed simulations to be described in a future paper suggest that water ice clouds can contribute sufficient radiative heating to yield a more isothermal temperature profile consistent with TES observations. There is general agreement between the modeled and observed pattern of the thermal tide fields; here defined as (T2pm-T2am). This field is strongly aliased by the limited diurnal monitoring by TES (twice daily), as described by *Wilson* [2000] and *Banfield et al.* [2003]. The limited vertical resolution of the TES nadir observations does contribute to a damping of the observed tide signature [*Banfield et al.*, 2003]. This is particularly likely in the tropics where the vertically propagating tide has a vertical wavelength that is readily smeared out by the TES retrieval. Figure 12e shows that the simulated dust distribution is strongly influenced the Hadley circulation, which is indicated by the mass transport stream function. The simulated vertically integrated column opacity is ∼0.8 in the tropics, which is high relative to observations. The column opacity is particularly weak at midlatitudes in the winter hemisphere.

[51] For L_s = 180° (Figure 13), there is again broad agreement in the diurnal-average temperature fields. In this case, the most notable difference is the tropical lapse rate. The diurnal tide fields are quite similar, with the observed field having about half the strength of the simulation. There is a cold temperature bias at both poles in the simulation at levels above ∼1 mb. The temperature field appears to suggest that the dust forcing is somewhat weak, as the simulated temperature distribution lacks the flat meridional distribution in the tropics that is evident in the observations. The mass transport stream function is quite weak relative to the solstitial case and the simulated dust field is somewhat more shallow. The optical column is similar in depth to that in the summer solstice simulation (Figure 12e). The opposite equinox (L_s = 360°, shown in Figure 15) is quite similar.

[52] For northern winter solstice (Figure 14), there is good qualitative agreement between the modeled and observed the temperature fields, but the simulated temperatures have a cold bias in the summer (southern) hemisphere that is most likely attributed to insufficient dust raising at the polar cap edge and in the southern polar latitudes generally (i.e., a similar deficiency in the vigor of small-scale dust storm lifting mentioned for northern summer). The meridional temperature gradient in the observed field is much stronger than that for the NH summer solstice season. The differences in the tide field is also consistent with greater dust heating at high southern latitudes in the observations than in the simulation. The total column opacity is greatest in this simulation, with a tropical max-

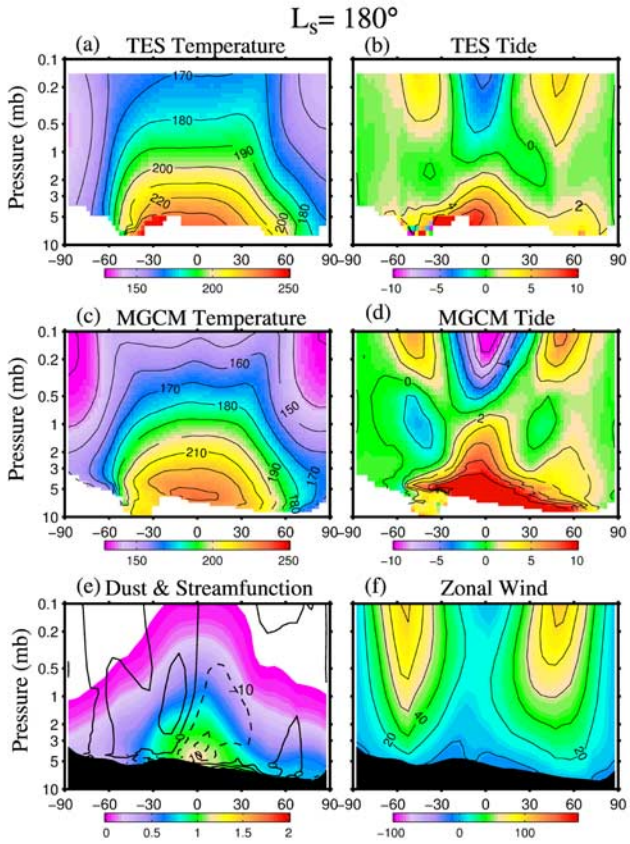

Figure 13. Same as Figure 12 but for L_s = 180°.

imum of ~1.2. The stream function is roughly double that in the summer solstice season. The dust distribution is deeper as well. The zonal wind field shows a subtropical jet in the southern hemisphere.

5.2. Spatial Pattern of Dust Devil Lifting and Dust Devil Occurrence Predictions

[53] To the extent that the model produces a good annual cycle, and does so with a dust injection scheme that is based on the thermodynamics of dust devils, the injection provides a prediction of the spatial distribution of dust devil activity. In Figures 16a, 16c, and 16e, we show diurnal-average maps of DDL dust injection at three different seasonal dates for the best fit scheme. A major trend in the position of predicted dust devil activity is due to the changing subsolar latitude with season. Figures 16a and 16c are close to northern and southern solstice, respectively, and show bands of dust devil activity that are biased in northward and southward directions, respectively. Figure 16e shows a map for L_s = 334°, which is significantly closer to equinox, and corresponds to more latitudinally uniform lifting. This broad-brush dependence on the subsolar latitude is entirely consistent with the assumed functional dependence of dust devil activity on peak solar heating (Figure 3).

[54] There is a great deal of spatial structure in the map for each season, beyond that simply due to latitude. The near-equinox pattern shown in Figure 16e is most directly interpretable. The sharp cutoff in lifting activity north of about 50°N is due to the presence of the seasonal CO_2 ice cap. The lifting scheme is designed not to lift dust when ice is present on the surface, and in any case, the drive for such lifting in the very strongly statically stable environment above the seasonal cap is negligible. At L_s = 334°, the subsolar latitude is still in the southern hemisphere; however, the peaks in dust devil activity are located in the north. These peaks all correspond to lower elevations where the pressure is higher and greater amounts of dust are able to be lifted. A secondary maximum of dust lifting occurs in a broken band just south of the equator; this corresponds to the subsolar latitude.

[55] The L_s = 120° output (Figure 16a) shows several peaks in dust devil lifting in the northern hemisphere. The largest of these peaks covers the Amazonis region (15°N–45°N, 170°E–140°W), which is encouraging, as this is the most vigorous region of dust devil activity observed on Mars [*Cantor and Edgett*, 2002; *Fisher et al.*, 2002]. Other peaks exist close to Elysium and on Lunae Planum and Acidalia. Dust devil lifting is a function of PBL top height and the sensible heat flux from the surface. Examination of the these components within the Amazonis peak (at 180°W) and at other longitudes with lower dust devil activity but similar surface pressure (90°E and 45°W) shows that the Amazonis peak is due to elevated sensible heat fluxes. While the peak PBL top height is roughly the same at all three locations (~4.5 km at this season), the sensible heat flux within Amazonis is nearly double that at the other two locations. This is directly ascribable to lower thermal inertia and 5–10K higher daytime temperatures within Amazonis at this season than at the other two longitudes.

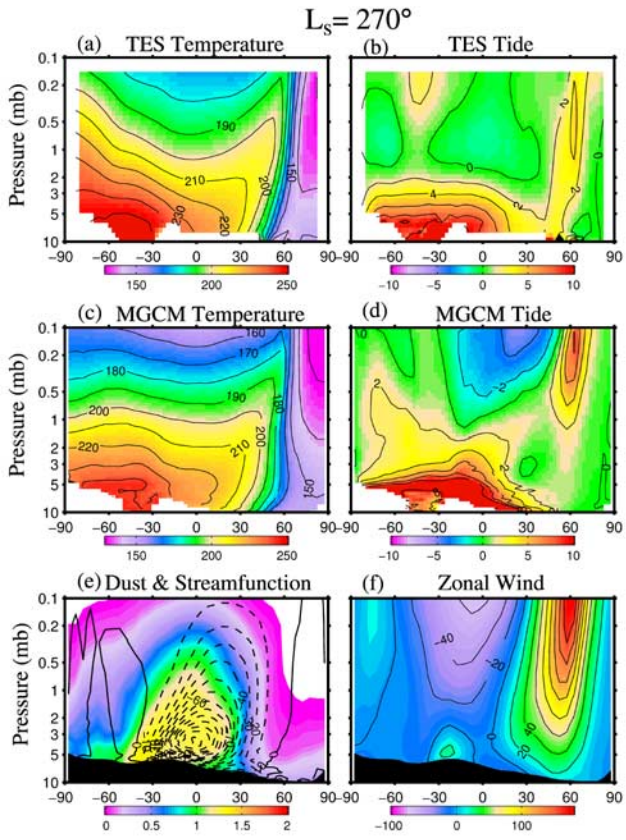

Figure 14. Same as Figure 12 but for L_s = 270°.

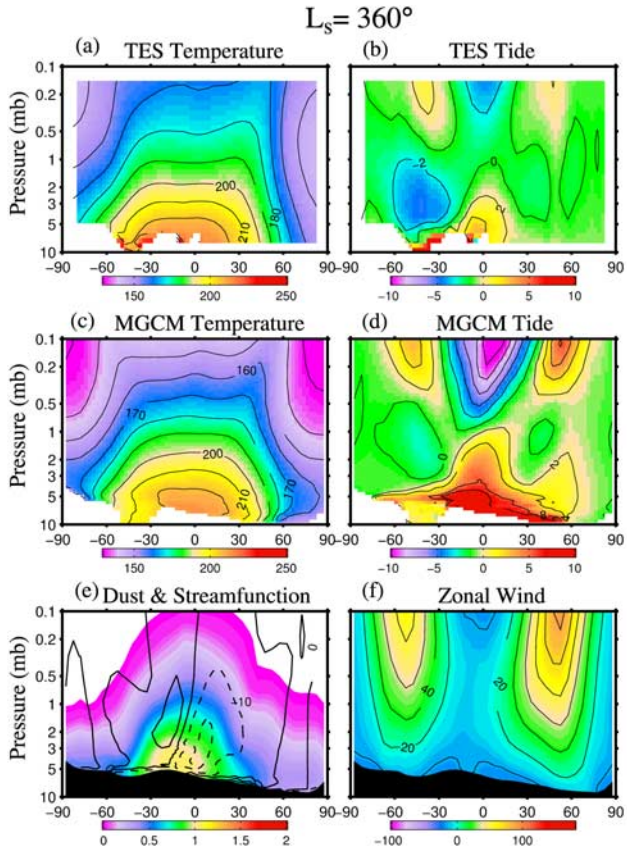

Figure 15. Same as Figure 12 but for L_s = 360°.

[56] Near southern solstice, the band of peak dust devil activity is biased to the southern hemisphere (Figure 16c). Significant localized peaks of dust devil activity are predicted in the southern tropics between 60°W and 60°E, and between 130°E and 120°W. Examination of the dust devil lifting function components suggest that neither the PBL height nor the surface temperatures are especially unusual within these regions, as compared to the gaps in dust devils activity in this belt, or compared to the regions just north and just south of the belts. Indeed, one interesting aspect of the L_s = 259° activity is that it maximizes in such a sharply confined zonal belt. This region coincides with the convergence zone of the Hadley circulation, and it is found that the critical factor in the elevated lifting is the enhanced sensible heat flux. This enhanced heat flux is directly ascribable to the high winds within this latitudinal band. Unlike the Amazonis dust devil activity, which peaked just afternoon along with surface temperatures, the southern tropical activity peaks in the late morning when winds are highest and the PBL is not yet full developed. The "dust devil" function in this case is capturing the effects of strong convective mixing of heat, but with strong mean winds, it is not clear whether this mixing would manifest itself as dust devils. Conventional wisdom suggests that dust devils may not be a preferred form of convection under conditions of high winds, while Large Eddy Simulation experiments suggest that dust devil formation may be insensitive to the strength of the background wind [*Toigo et al.*, 2003]. The L_s = 259° output may also be compared with the "season 10" output (L_s = 270°–300°) shown by *Newman et al.* [2002a]. The band of dust devil activity found here is similar to that found by *Newman et al.* [2002a], save for the fact that the band in this study is wider in latitude and less longitudinally uniform.

[57] Figure 16 also includes panels that show the net lifting (over a diurnal cycle) of dust for the same seasons as the dust devil injection output (Figures 16b, 16d, and 16f). "Net" in this case refers to the resultant effects of injection and gravitational settling of dust (there is no mean wind stress lifting in this simulation). Thus, if dust is injected during the day, but falls out at the same location at night, there is no net injection. The net injection can also be negative for regions that are net dust sinks for the seasonal dates shown. The net injection is compared with the dust devil injection to assess the degree to which patterns of dust fallout, and the ability of the atmosphere to export dust from different regions, causes differences in the spatial patterns of "gross" and "net" dust supply of dust.

[58] The near equinox case (Figure 16f, L_s = 334°) shows the largest areas of sign change between convective and net injection. Large regions of Tharsis, Arabia, and Sabaea show positive convective injections (predicted dust devil activity), yet they exhibit net accumulation of dust. These large areas provide a good example of the need to use predictions of the dust devil injection component, rather than the net injection, to predict dust devil activity from the model.

[59] The two more nearly solstitial simulations (Figures 16b and 16d, L_s = 120° and 259°) show net deposition of dust on the seasonal CO_2 ice deposits, while all three frames show net deposition of dust in the majority of Hellas. This strong and nearly continuous deposition of material may be an important link in the cycle of large-scale dust storm activity, as discussed by B04. The southern solstitial simulation provides an example of the differing efficiency of dust injection at different locations. In the southern high latitudes (<60°S), a very high percentage (30–100%, depending on exact location) of the dust injected during the brief period of daytime dust devil action is lost from the surface. This suggests very efficient removal by atmospheric transport from these locations. Conversely, in the lower northern midlatitudes, similar rates of dust devil activity correspond to net deposition of dust. Figure 16c and output for times a little later in southern spring and summer suggest that dust devil activity would have been observed even at the high latitude of the Mars Polar Lander (75°S), and as indicated in MOC imagery.

[60] The GCM results suggest that dust devils should occur at some point in the day, and at some locations within the area defined by each GCM grid box, for essentially all non-ice-covered locations on the planet. The average northern summer dust injection required by the model is about 2×10^{-5} g cm^{-2} sol^{-1} (Figure 9). This can be compared with the lifting capacity of a typical dust devil derived from Mars Pathfinder observations by *Ferri et al.* [2003] of 7×10^{-5} kg m^{-2} s^{-1} or 0.62 g cm^{-2} sol^{-1}. Assuming dust devils are active for only a quarter of the day, the fractional area of dust devil activity required by the model is roughly 1.3×10^{-4}, which is very close to the 2×10^{-4} estimated by *Ferri et al.* [2003], again on the basis of the Imager for Mars Pathfinder observations. As such, the model predicted

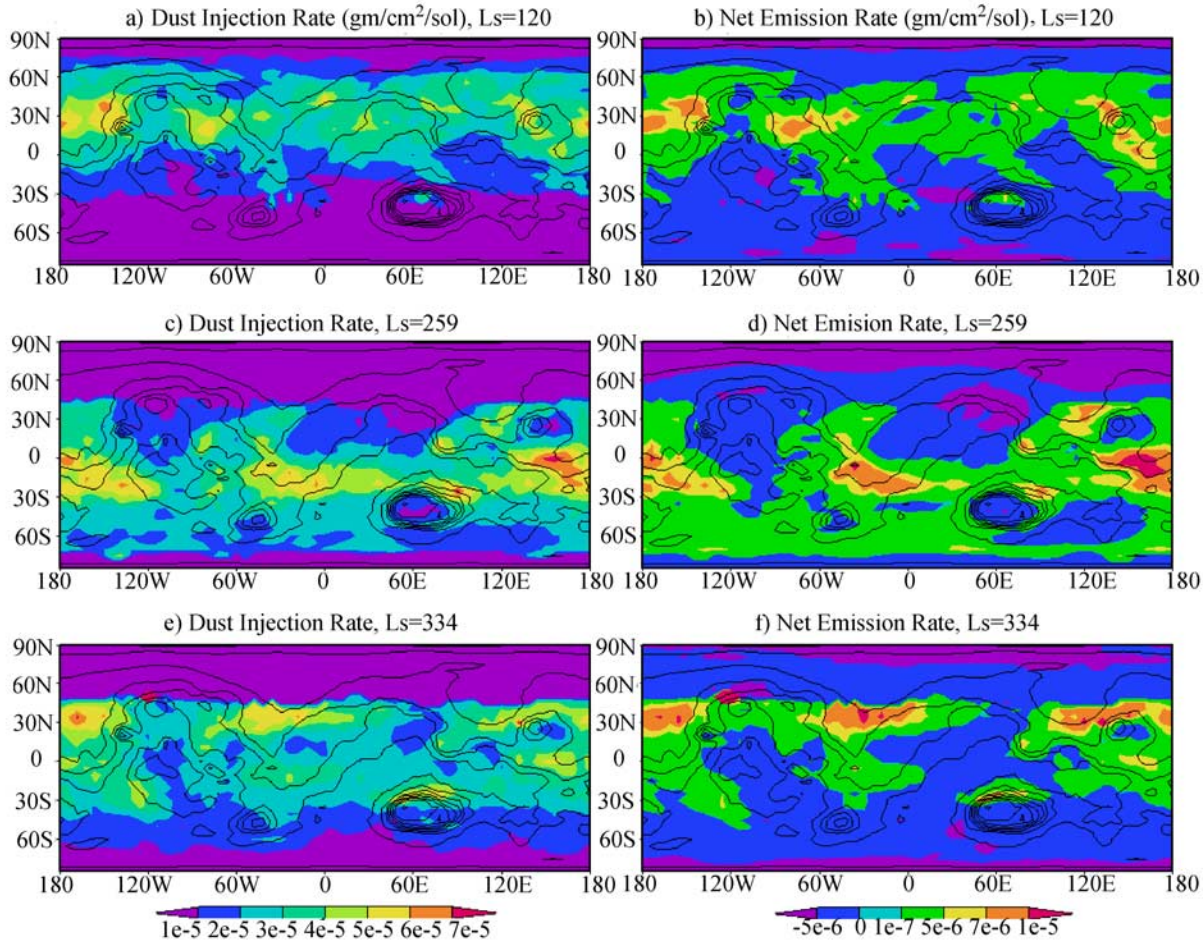

Figure 16. The relationship between (a, c, and e) diurnal mean injection of dust by dust devils and (b, d, and f) the net emission of dust from the surface (the residual between lifting and fallout). Maps are shown for L_s = 120°, 259°, and 334°. The net emission values are about a factor of three lower than the dust devil injection. The spatial patterns are quite similar. Note the peak in dust devil activity over Amazonis in northern summer, which is consistent with a high abundance of Mars Orbiter Camera images of dust devils in this region.

dust devil activity area and required dust devils per unit area are consistent with observations.

5.3. Prediction of Local and Regional Dust Storm Activity

[61] The presence of an interactive dust-lifting scheme allows the model to generate predictions of the number and spatial distribution of local and regional dust storm events (scales greater than 10^5 km). This model prediction allows the *Cantor et al.* [2001] dust storm catalog to be directly used to constrain a GCM simulation. Previous studies have used model-predicted stress patterns to compare with the observed storm occurrence [*Haberle et al.*, 2003; C. E. Newman et al., The atmospheric circulation and dust activity in different orbital epochs on Mars, submitted to *Icarus*, 2004 (hereinafter referred to as Newman et al., submitted manuscript, 2004)]. Figure 17a shows a map of the origin locations of local and regional dust storms in the "best fit" simulation. The model output is available for all times of year, while the published catalog covers the period from L_s = 109°–274°, but otherwise Figure 17a and the *Cantor et al.* [2001] Plate 1 can be directly compared (the data from *Cantor et al.* [2001] have been plotted as Figure 17b, for easier comparison with the model output). Major, "broad-brush" agreement between the model and data include the general paucity of storms over the regions centered on Terra Meridiani (0°N, 0°W), Tharsis (0°N, 120°W), and Hesperia (0°N, 120°E), and the elevated dust storm activity in the mid to high latitudes of both hemispheres (>40°N, <40°S). The GCM appears to underpredict cap-edge dust storm activity, especially at the very high latitudes. However, investigation of the dust opacity and surface wind stress output suggest that very high latitude (>60°) localized high wind stress events do occur, but that the polar Fourier filter prevents the development of sharp, localized dust opacity maxima, which was the basis of the dust storm identification method used to construct Figure 17. (Fourier filtering is needed in grid point GCMs to prevent computational instability as the longitudinal grid points converge toward the pole; all current, published Mars GCMs are grid point models, except for the Oxford Mars GCM [*Read et al.*, 1997; *Newman et al.*, 2002a, 2002b].)

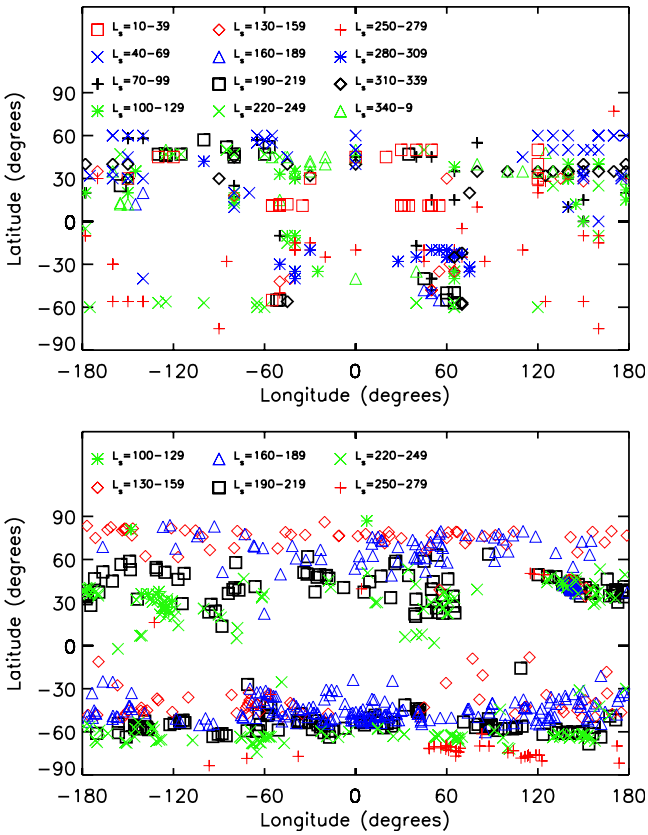

Figure 17. The spatial distribution of the origin locations of local and regional dust storms (a) as predicted by the "best fit" GCM simulation and (b) as observed in MOC WA images [*Cantor et al.*, 2001]. Note that while the minimum dust storm size detectable by MOC in this survey was about 60 km^2, the GCM grid box size is 108,000 km^2.

[62] The model appears to somewhat overpredict dust storm activity in Hellas and Argyre, although this is more likely a reflection of underprediction of events at other latitudes in the southern midlatitudes. This can be verified by comparing the number of events in Hellas within a given seasonal bin (say, L_s = 190°–219°), during which the model predicts 5 events in and around Hellas, while *Cantor et al.* [2001] count over 20. The model predicts a peak in local events in (and to the north of) Hellas during L_s = 280°–309°, after the end of the *Cantor et al.* [2001] study period. Some of the offset in storm numbers is likely due to the smallest resolvable dust storm size in the GCM (1.08 × 10^5 km^2) being larger than a good fraction of the *Cantor et al.* [2001] storms. The effect of resolution, especially in critical regions such as the high-latitude seasonal cap edge zones needs to be studied further in the future.

[63] Noticeable increases in storm activity can be seen in the northern midlatitudes in the seasonal bins near the equinoxes. A distinct spatial pattern to the distribution of these storms can be seen, with three "fingers" of activity dipping to lower latitudes near 50°W, 80°E, and 160°E. These are locations where baroclinic storm activity peaks [*Hollingsworth et al.*, 1996], and also correspond to the "flushing channels" where these storms can become entrained in the tropical circulation, transporting dust to lower latitudes, as discussed by *Wang et al.* [2003]. The predicted peaks in activity correspond reasonably well with the observations [*Cantor et al.*, 2002]. Additional mid northern latitude storm activity is predicted over eastern Amazonis (150°W), in correspondence with observations. This lifting is apparently associated with the sharp topographic gradient as the Amazonis lowlands rapidly grade into the flank of Olympus Mons and the Tharsis plateau.

6. Spatial Distribution of Net Dust Lifting and Deposition

[64] Prognostic simulation of the full annual atmospheric dust cycle allows us to examine the fluxes of significance for the Martian surface dust deposits in a manner that has not been possible to date. Large areas of thick dust mantling have been identified mapped using thermal and visible remote sensing [*Christensen*, 1986]. Ultimately, these "dust continents" must result from an imbalance of dust erosion and deposition on a timescale that depends strongly on the deposition/erosion rates. Since the prediction of net deposition/erosion rates requires prediction of dust lifting by wind stress and by convective dust devils, dust transport by the model winds, and the patterns of dust fallout, prior predictions of deposition/erosion rates have been incomplete [e.g., *Haberle et al.*, 2003].

[65] Figure 18 shows the annually integrated, net dust erosion depth for the "best case" simulation described in the previous section. This simulation includes dust devil and wind stress lifting, and comes from a simulation that generates variable global dust storms. The year shown does not include a global dust storm. Similar output for a year with a global dust storm is described by B04. The figure shows that across the tropics and midlatitudes there is a near balance of lifting and deposition: regions of similar areas exhibit similar magnitudes of lifting, but with opposite signs, suggesting patterns of net regional dust transport. For example, strong winds in the Chryse region (30°–60°W), which are generated by concentration of the Hadley cell return flow, generate strong net lifting. Net deposition occurs on the high Tharsis Plateau (80°–120°W, 30°S–10°N). In general, the annual amounts of dust deposition/erosion are smaller than about 10 μm, and the average over the tropics and midlatitudes is over an order of magnitude smaller than this. The maximum settling rates in the tropics and midlatitudes are at the lower end of the *Pollack et al.* [1979] and the *Landis and Jenkins* [2000] estimates of mean fallout, and somewhat higher than estimated by *Cantor et al.* [2001]. A large fraction of the planet that experiences deposition does so at rates about an order of magnitude smaller than this (~1–5 μm/Martian year). This rate is nearer to, but still about an order of magnitude higher than, settling rate estimates from the fading of slope streaks (~0.3 μm/Martian year) [*Aharonson et al.*, 2003] (while the spatial mean value of about 0.3 μm/year is very close to this estimate, the GCM predicts significant net dust erosion in the region of Amazonis where the longest baseline of observations for this deposition estimate were available). The *Landis and Jenkins* [2000] observations are not for a full year; when we examine fallout for the Mars Pathfinder operational period relevant to that study (L_s = 142°–160°), we find an equivalent annual rate of about 10 μm/year

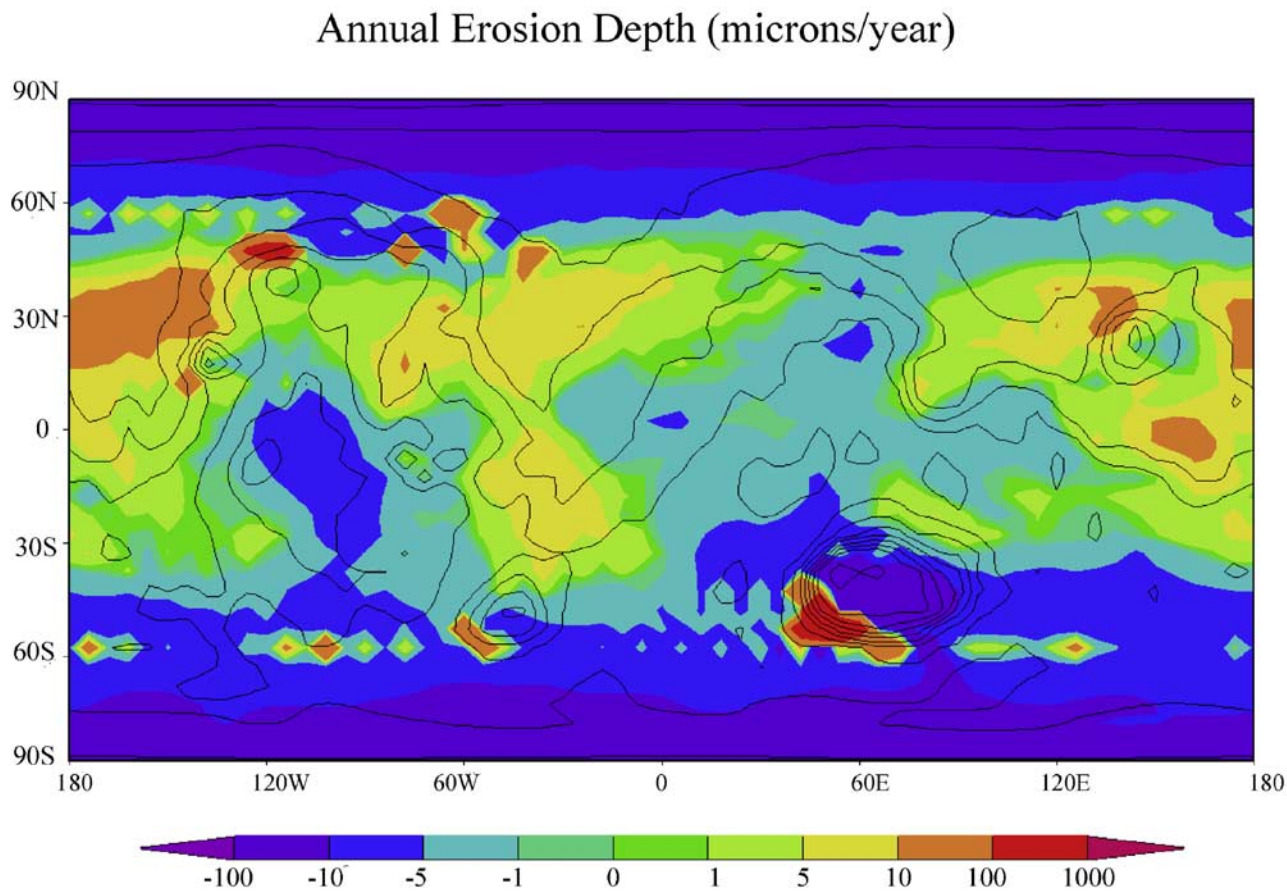

Figure 18. The GCM-predicted, annually integrated net dust erosion depth (μm/year) for the "best fit" case. The topography is contoured in black for context.

versus the *Landis and Jenkins* [2000] measurement of 6 μm/year. Finally, the *Pollack et al.* [1979] and the *Cantor et al.* [2001] estimates were based on consideration of dust fallout following the 1977 dust storms and fallout from observed regional storms only. The applicability to fallout of dust generated by all sources is questionable. The GCM peak net injection rates (~10 μm/Martian year) are about three orders of magnitude smaller than the "erosion potential" estimates calculated by *Haberle et al.* [2003], but similar to values obtained by Newman et al. (submitted manuscript, 2004). About an order of magnitude's worth of this discrepancy is ascribable to the difference between instantaneous dust injection and instantaneous dust injection minus dust fallout. Most of the remainder is due to the fact that as the seasons change, the regions of instantaneous dust injection change. As a result, areas of strong net lifting at, say, L_s = 120° become regions of deposition at other seasons. The "erosion potential" takes into account neither of these factors of deposition, and thus if interpreted as the net dust injection or erosion rate (which *Haberle et al.* [2003] warn against doing), it is grossly in error.

[66] Averaged between 75°S and 75°N, the net annual effect for current orbital parameters is one of erosion; a very small amount of dust is removed each year, corresponding to much less than 1 μm (~0.3 μm to be exact, but an estimate of 0.1–1 μm probably better captures uncertainties). Net loss over most of the planet is required by net deposition at both poles, as discussed by *Pollack et al.* [1979]. The net deposition at the poles proceeds in the simulation at roughly 20 μm/Martian year. This rate approaches the dust-settling rate estimated by *Pollack et al.* [1979] of 10–40 μm. This deposition rate is uniform (to the factor of a few level) over the seasonal and residual caps, so a dust deposition rate onto the residual caps of roughly this rate (10–20 μm/year) is our best estimate for consideration, say, of dust incorporation for models of layered deposit formation.

[67] The pattern and rates of dust deposition/erosion shown in Figure 16 are problematic for the development and maintenance of the low-latitude "dust continents." The model predicts a distinct pattern of net erosion and net deposition at a sufficient rate that deposits of dust over 100m thick could be formed. This is likely much thicker than many of the actual deposits, which have been observed to undergo geographical redistribution on timescales of a few Martian years. Further, the spatial pattern of predicted dust deposition/erosion does not correlate perfectly with the observed distribution of dust deposits. *Christensen* [1986] discussed the possibility of redistribution of the surface dust deposits over time as the circulation changed with changing spin/orbital properties (obliquity, eccentricity, and argument of perihelion). Such changes require deposition/erosion

rates of ~10 μm/year, which are not far from the higher values found over a good fraction (maybe a quarter) of the planet between 50°S and 50°N.

7. Summary and Conclusions

[68] This paper presents results from GCM simulations of an interactive dust cycle on Mars. The version of the GFDL Mars GCM used in this study differs from that described by *Fenton and Richardson* [2001], *Richardson and Wilson* [2002], *Richardson et al.* [2002], and *Mischna et al.* [2003]. Instead of a dust injection scheme based only on the surface-air temperature contrast, the present model includes detailed, physically based parameterizations of dust lifting, similar to the approach of *Newman et al.* [2002a]. These schemes represent the injection of dust by convective motions, using thermodynamic theory of dust devils [*Renno et al.*, 1998, 2000], applied on the coarse resolution of the GCM grid, and by large-scale wind stresses, using a functional dependence on the frictional velocity [*Shao*, 2001]. As before, the model treats dust as a transportable trace species, the dust distribution being affected by the model-resolved winds, subgrid-scale diffusion, and particle-mass-dependent sedimentation. The dust is radiatively active in the GCM, influencing thermal infrared and visible radiative heating of the atmosphere.

[69] The convective and resolved-wind dust injection schemes introduce three free parameters. A given simulation, extending for multiple Martian years, uses spatially and temporally fixed values for each of these free parameters. These parameters are the rate constants applied to the two injection schemes (simple multipliers) and the threshold lifting stress for the resolved-wind lifting scheme. Convective lifting is prescribed without a threshold. We chose to use the seasonal cycle of globally averaged air temperatures as our primary quantitative means of assessing the quality of the GCM simulations. The first question we address with the model is whether the injection schemes can generate a dust cycle in agreement with observations, and what combination(s) of parameters allow the best fit. We find that the shape of the seasonal air temperature curve in northern spring and summer, when air temperatures are observed to be highly repeatable [*Liu et al.*, 2003], can be fit either by the convective lifting scheme or by the stress-lifting scheme with low values of stress-threshold and lifting rate. The northern spring and summer temperatures cannot be fit if the dust opacity only results from the fallout of dust from a global storm in the previous southern summer. Both the convective and low-threshold stress-lifting schemes require steady and widespread dust lifting throughout northern spring and summer. Widespread convective (dust devil) lifting seems consistent with the widespread observation of dust devils and dust devil tracks, and indeed the model predicts injection rates that are in good agreement with analysis of Imager for Mars Pathfinder data [*Ferri et al.*, 2003]. Widespread wind stress lifting seems much less consistent with the relatively few and sporadic local dust storms observed in northern summer [*Cantor et al.*, 2001]. Specifically, cap edge storms, other local dust storms, and lifting associated with dust streak formation appear insufficiently frequent. Further work is needed to provide quantitative support for these qualitative arguments. However, on the basis of the model results and inferences from observations, we propose that dust devils are the primary dynamical system providing the dust injection necessary to sustain the background haze on Mars.

[70] Regardless of the convective scheme rate parameter, dust storms cannot be generated in the model. From this we suggest that dust devils are not the precursors of dust storms, in agreement with imaging observations. It is also not possible to generate dust storms with the stress-lifting scheme set with parameter values necessary to sustain the background dust haze. Conversely, with stress values and injection rates high enough to initiate storm activity, lifting does not occur throughout much of northern spring and summer. Simulation of the dust cycle involving storms and the background haze requires two schemes: a combination of high-rate, high-threshold lifting, and either convective lifting or low-threshold, low-rate stress lifting. Justification for the use of two different sets of injection parameters in two parallel stress-lifting schemes is possible, but seems a more complex and observationally less-well supported solution than the convective plus high-threshold injection scheme option. When run with a combination of convective and high-threshold dust injection schemes, the model is able to generate both a realistic background dust cycle, and for the first time, spontaneous and interannually (and intra-annually) variable global dust storms. These storms are discussed in greater detail by B04.

[71] Varying injection parameters, a multiyear "best fit" simulation can been produced with optimal air temperature and dust storm emulation. This simulation uses convective and high-threshold stress lifting. The model develops a range of local and regional storms, the variety and distribution of which compares reasonably well with observations [*Cantor et al.*, 2001]. Specifically, seasonal ice-cap edge dust storms are simulated, as are storms associated with various topographic features. Comparison with air temperature cross section data suggest that cap edge lifting is somewhat underpredicted. Several small dust storms are generated in the northern early autumn and later winter, associated with low-pressure frontal storms, as described by *Wang et al.* [2003], and also generated in the Oxford Mars GCM [*Newman et al.*, 2002b]. One such storm develops into a large regional event, resembling the 1999 storm and the dust storm that preceded the Mars Exploration Rover landings (B04). The model also predicts the distribution and seasonal variation of dust devil activity (if the convective lifting is ascribed to dust devils). A distinct peak in activity is found in the model in Amazonis, a region of observed enhanced dust devil activity.

[72] The rates of dust injection and the net removal/deposition of dust on the surface are predictions of the model. It has not been possible to predict annually integrated net dust deposition/erosion rates until this point as it requires a validated dust cycle that includes interactive lifting, transport, and deposition of dust. Previous estimates of dust erosion have had to rely on "lifting potential" derived from the model wind stresses to predict lifting and have ignored the other side of the cycle: deposition [*Haberle et al.*, 2003]. Our results suggest that net, annually integrated erosion/deposition rates are roughly one to two orders of magnitude lower when the full dust cycle is taken into account. Thus extreme caution must be taken when

interpreting the previously generated "lifting potential" erosion values. Net annual erosion/deposition rates compare well with estimates from the Mars Pathfinder solar panel experiment [*Landis and Jenkins*, 2000] and from analysis of the darkening of slope streaks [*Aharonson et al.*, 2003]. Between 75°S and 75°N, the net annual erosion rate is 0.3 μm/Martian year (0.1–1 μm/Martian year, conservatively), which is balanced by net polar deposition at roughly 20 μm/Martian year, consistent with estimates from *Pollack et al.* [1979]. Although these values are the best possible GCM estimate at this time, the model still neglects processes of potential importance, including dust-ice interactions. These must be assessed in future models.

[73] **Acknowledgments.** S.B. and M.I.R. were supported by NSF Planetary Astronomy Award number 0406653. R.J.W. was supported by the NASA Planetary Atmospheres program grant. We thank our referees, Richard Zurek and anonymous reviewer, for useful suggestions. We also thank Claire E. Newman and A. P. Ingersoll for useful discussions.

References

Aharonson, O., N. Schorghofer, and M. F. Gerstell (2003), Slope streak formation and dust deposition rates on Mars, *J. Geophys. Res.*, *108*(E12), 5138, doi:10.1029/2003JE002123.

Balme, M. R., P. L. Whelley, and R. Greeley (2003), Mars: Dust devil track survey in Argyre Planitia and Hellas Basin, *J. Geophys. Res.*, *108*(E8), 5086, doi:10.1029/2003JE002096.

Banfield, D., et al. (2003), Forced waves in the Martian atmosphere from MGS TES nadir data, *Icarus*, *161*, 319–345.

Briggs, G. A., W. A. Baum, and J. Barnes (1979), Viking Orbiter imaging observations of dust in the Martian atmosphere, *J. Geophys. Res.*, *84*, 2795–2820.

Cantor, B. A., and K. S. Edgett (2002), Martian dust devils: 2 Mars years of MGS MOC observations, *Eos Trans. AGU*, *83*(47), Fall Meeting Suppl., Abstract P51A-0331.

Cantor, B. A., P. B. James, M. Caplinger, and M. J. Wolff (2001), Martian dust storms: 1999 Mars Orbiter Camera observations, *J. Geophys. Res.*, *106*, 23,653–23,687.

Cantor, B., M. Malin, and K. S. Edgett (2002), Multiyear Mars Orbiter Camera (MOC) observations of repeated Martian weather phenomena during the northern summer season, *J. Geophys. Res.*, *107*(E3), 5014, doi:10.1029/2001JE001588.

Christensen, P. R. (1986), Regional dust deposits on Mars: Physical properties, age and history, *J. Geophys. Res.*, *91*, 3533–3545.

Clancy, R. T., D. O. Muhleman, and G. L. Berge (1990), Global changes in the 0–70 km thermal structure of the Mars atmosphere derived from 1975 to 1989 microwave CO spectra, *J. Geophys. Res.*, *95*, 14,543–14,554.

Clancy, R. T., A. W. Grossman, M. J. Wolff, P. B. James, D. J. Rudy, Y. N. Billawala, B. J. Sandor, S. W. Lee, and D. O. Muhleman (1996), Water vapor saturation at low altitudes around Mars aphelion: A key to Mars climate?, *Icarus*, *122*, 36–62.

Clancy, R. T., B. J. Sandor, M. J. Wolff, P. R. Christensen, M. D. Smith, J. C. Pearl, B. J. Conrath, and R. J. Wilson (2000), An intercomparison of ground-based millimeter, MGS TES, and Viking atmospheric temperature measurements: Seasonal and interannual variability of temperatures and dust loading in the global Mars atmosphere, *J. Geophys. Res.*, *105*(E4), 9553–9572.

Colburn, D. S., J. B. Pollack, and R. M. Haberle (1989), Diurnal variations in optical depth at Mars, *Icarus*, *79*, 159–189.

Conrath, B. J., J. C. Pearl, M. D. Smith, W. C. Maguire, P. R. Christensen, S. Dason, and M. S. Kaelberer (2000), Mars Global Surveyor Thermal Emission Spectrometer (TES) observations: Atmospheric temperatures during aerobraking and science phasing, *J. Geophys. Res.*, *105*, 9509–9519.

Fenton, L. K., and M. I. Richardson (2001), Martian surface winds: Insensitivity to orbital changes and implications for aeolian processes, *J. Geophys. Res.*, *106*, 32,885–32,902.

Fenton, L. K., J. C. Pearl, and T. Z. Martin (1997), Mapping Mariner 9 dust opacities, *Icarus*, *130*, 115–124.

Ferri, F., P. H. Smith, M. Lemmon, and N. O. Rennó (2003), Dust devils as observed by Mars Pathfinder, *J. Geophys. Res.*, *108*(E12), 5133, doi:10.1029/2000JE001421.

Fisher, J., et al. (2002), A survey of Martian dust devil activity using Mars Global Surveyor Mars Orbiter camera images, *Eos Trans. AGU*, *83*(47), Fall Meet. Suppl., Abstract P01-5742.

Forget, F., F. Hourdin, R. Fournier, C. Hourdin, O. Talagrand, M. Collins, S. R. Lewis, P. L. Read, and J. P. Huot (1999), Improved general circulation model of the Martian atmosphere from the surface to above 80 km, *J. Geophys. Res.*, *104*, 24,155–24,175.

Gierasch, P. J., and R. M. Goody (1968), A study of the thermal and dynamical structure of the Martian lower atmosphere, *Planet. Space Sci.*, *16*, 615–646.

Greeley, R., N. Lancaster, S. Lee, and P. Thomas (1992), Martian Aeolian processes, sediments and features, in *Mars*, edited by H. H. Kieffer et al., pp. 730–776, Univ. of Ariz. Press, Tucson.

Haberle, R. M., J. B. Pollack, J. R. Barnes, R. W. Zurek, C. B. Leovy, J. R. Murphy, H. Lee, and J. Schaeffer (1993), Mars atmospheric dynamic circulation as simulated by the NASA Ames general circulation model: The zonal mean circulation, *J. Geophys. Res.*, *98*, 3093–3123.

Haberle, R. M., J. R. Murphy, and J. Schaeffer (2003), Orbital change experiments with a Mars general circulation model, *Icarus*, *161*, 66–89.

Hamilton, K. (1995), Interannual variability in the northern hemisphere winter middle atmosphere in control and perturbed experiments with the GFDL SKYHI general circulation model, *J. Atmos. Sci.*, *52*, 44–66.

Hanel, R. C., et al. (1972), Investigation of Martian environment by infrared spectroscopy on Mariner 9, *Icarus*, *17*, 423–442.

Hinson, D. P., and R. J. Wilson (2002), Transient eddies in the southern hemisphere of Mars, *Geophys. Res. Lett.*, *29*(7), 1154, doi:10.1029/2001GL014103.

Hinson, D. P., and R. J. Wilson (2004), Temperature inversions, thermal tides, and water ice clouds in the Martian tropics, *J. Geophys. Res.*, *109*, E01002, doi:10.1029/2003JE002129.

Hollingsworth, J. L., R. M. Haberle, J. R. Barnes, A. F. C. Brider, J. B. Pollack, H. Lee, and J. Schaeffer (1996), Orographic control of storm zones on Mars, *Nature*, *380*, 413–416.

Kahn, R. A., T. Z. Martin, R. W. Zurek, and S. W. Lee (1992), The Martian dust cycle, in *Mars*, edited by H. H. Kieffer et al., pp. 1017–1053, Univ. of Ariz. Press, Tucson.

Kieffer, H. H., and A. P. Zent (1992), Quasi-periodic climate change on Mars, in *Mars*, edited by H. H. Kieffer et al., pp. 1180–1220, Univ. of Ariz. Press, Tucson.

Landis, G. A., and P. P. Jenkins (2000), Measurement of the settling rate of atmospheric dust on Mars by the MAE instrument on Mars Pathfinder, *J. Geophys. Res.*, *105*, 1855–1857.

Leovy, C. B., G. Briggs, A. Young, B. Smith, J. Pollack, E. Shipley, and R. Widley (1972), The Martian atmosphere: Mariner 9 television experiment progress report, *Icarus*, *17*, 373–393.

Liu, J., M. I. Richardson, and R. J. Wilson (2003), An assessment of the global, seasonal, and interannual spacecraft record of Martian climate in the thermal infrared, *J. Geophys. Res.*, *108*(E8), 5089, doi:10.1029/2002JE001921.

Lorenz, R. D., J. I. Lunine, J. A. Grier, and M. A. Fisher (1996), Martian surface wind speeds described by the Weibull distribution, *J. Spacecr. Rockets*, *33*, 754–756.

Magalhaes, J. A., and R. E. Young (1995), Downslope windstorms in the lee of ridges on Mars, *Icarus*, *113*, 277–294.

Malin, M., and K. S. Edgett (2001), Mars Global Surveyor Mars Orbiter Camera: Interplanetary cruise through primary mission, *J. Geophys. Res.*, *106*, 23,429–23,570.

Martin, L. J., and R. W. Zurek (1993), An analysis of the history of dust activity on Mars, *J. Geophys. Res.*, *98*, 3221–3246.

Martin, T. Z. (1981), Mean thermal and albedo behavior of the Mars surface and atmosphere over a Martian year, *Icarus*, *45*, 427–446.

Martin, T. Z. (1986), Thermal Infrared opacity of the Mars atmosphere, *Icarus*, *66*, 2–21.

Martin, T. Z., and H. H. Kieffer (1979), Thermal infrared properties of the Martian atmosphere: 2. The 15-μm band measurements, *J. Geophys. Res.*, *84*, 2843–2852.

Martin, T. Z., and M. I. Richardson (1993), New dust opacity mapping from Viking infrared thermal mapper data, *J. Geophys. Res.*, *98*, 10,941–10,949.

Metzger, S. M., J. R. Carr, J. R. Johnson, T. J. Parker, and M. T. Lemmon (1999), Dust devil vortices seen by Mars Pathfinder Camera, *Geophys. Res. Lett.*, *26*, 2781–2784.

Mischna, M. A., M. I. Richardson, R. J. Wilson, and D. J. McCleese (2003), On the orbital forcing of Martian water and CO_2 cycles: A general circulation model study with simplified volatile schemes, *J. Geophys. Res.*, *108*(E6), 5062, doi:10.1029/2003JE002051.

Moore, H. J. (1985), The Martian dust storm of Sol-1742, *Proc. Lunar Planet. Sci. Conf. 16th*, Part 1, *J. Geophys. Res.*, *90*, suppl., D163–D174.

Murphy, J. R., and S. Nelli (2002), Mars Pathfinder convective vortices: Frequency of occurrence, *Geophys. Res. Lett.*, *29*(23), 2103, doi:10.1029/2002GL015214.

Murphy, J. R., O. B. Toon, R. M. Haberle, and J. B. Pollack (1990), Numerical simulations of the decay of Martian global dust storms, *J. Geophys. Res.*, *95*, 14,629–14,648.

Newman, C. E., S. R. Lewis, P. L. Read, and F. Forget (2002a), Modeling the Martian dust cycle, 1. Representations of dust transport processes, *J. Geophys. Res.*, *107*(E12), 5123, doi:10.1029/2002JE001910.

Newman, C. E., S. R. Lewis, P. L. Read, and F. Forget (2002b), Modeling the Martian dust cycle 2. Multiannual radiatively active dust transport simulations, *J. Geophys. Res.*, *107*(E12), 5124, doi:10.1029/2002JE001920.

Pollack, J. B., D. Colburn, F. M. Flasar, R. Kahn, C. E. Carlston, and D. Pidek (1979), Properties and effects of dust particles suspended in the Martian atmosphere, *J. Geophys. Res.*, *84*, 2929–2945.

Read, P. L., M. Collins, F. Forget, R. Fournier, F. Hourdin, S. R. Lewis, O. Talagrand, F. W. Taylor, and N. P. J. Thomas (1997), A GCM climate database for Mars: For mission planning and scientific studies, *Adv. Space Res.*, *19*, 1213–1222.

Renno, N. O., M. L. Burket, and M. P. Larkin (1998), A simple thermodynamic theory for dust devils, *J. Atmos. Sci.*, *55*, 3244–3252.

Renno, N. O., A. A. Nash, J. Lunine, and J. Murphy (2000), Martian and terrestrial dust devils: Test of a scaling theory using Pathfinder data, *J. Geophys. Res.*, *105*, 1859–1865.

Richardson, M. I. (1998), Comparison of microwave and infrared measurements of Martian atmosphere temperatures: Implications for short term climate variability, *J. Geophys. Res.*, *103*, 5911–5918.

Richardson, M. I., and R. J. Wilson (2002), Investigation of the nature and stability of the Martian seasonal water cycle with a general circulation model, *J. Geophys. Res.*, *107*(E5), 5031, doi:10.1029/2001JE001536.

Richardson, M. I., R. J. Wilson, and A. V. Rodin (2002), Water ice clouds in the Martian atmosphere: General circulation model experiments with a simple cloud scheme, *J. Geophys. Res.*, *107*(E9), 5064, doi:10.1029/2001JE001804.

Seguro, J. V., and T. W. Lambert (2000), Modern estimation of the parameters of the Weibull wind speed distribution for wind energy analysis, *J. Wind Eng. Ind. Aerodyn.*, *85*, 75–84.

Shao, Y. (2001), *Physics and Modeling of Wind Erosion*, pp. 113–316, Kluwer Acad., Norwell, Mass.

Smith, M. D. (2004), Interannual variability in TES atmospheric observations of Mars during 1999–2003, *Icarus*, *167*, 148–165.

Smith, M. D., J. C. Pearl, B. J. Conrath, and P. R. Christensen (2001), Thermal Emission Spectrometer results: Mars atmospheric thermal structure and aerosol distribution, *J. Geophys. Res.*, *106*, 23,929–23,945.

Smith, M. D., R. J. Conrath, J. C. Pearl, and P. R. Christensen (2002), Thermal Emission Spectrometer observations of Martian planet encircling dust storm 2001A, *Icarus*, *157*, 259–263.

Smith, P. H., and M. Lemmon (1999), Opacity of the Martian atmosphere measured by the images from Mars Pathfinder, *J. Geophys. Res.*, *104*, 8975–8985.

Thomas, P., and P. J. Gierasch (1985), Dust devils on Mars, *Science*, *230*, 175–177.

Thomas, P., J. Veverka, S. Lee, and A. Bloom (1981), Classification of wind streaks on Mars, *Icarus*, *45*, 124–153.

Thomas, P., J. Veverka, D. Gineris, and L. Wong (1984), Dust streaks on Mars, *Icarus*, *60*, 161–179.

Thomas, P. C., P. Gierasch, R. Sullivan, D. S. Miller, E. A. del Castillo, B. Cantor, and M. T. Mellon (2003), Meso-scale linear streaks on Mars: Environments of dust entrainment, *Icarus*, *162*, 242–258.

Toigo, A. D., and M. I. Richardson (2000), Seasonal variation of aerosols in the Martian atmosphere, *J. Geophys. Res.*, *105*, 4109–4121.

Toigo, A. D., M. I. Richardson, S. P. Ewald, and P. J. Gierasch (2003), Numerical simulation of Martian dust devils, *J. Geophys. Res.*, *108*(E6), 5047, doi:10.1029/2002JE002002.

Wang, H., M. I. Richardson, R. J. Wilson, A. P. Ingersoll, A. D. Toigo, and R. W. Zurek (2003), Cyclones, tides, and the origin of a cross-equatorial dust storm on Mars, *Geophys. Res. Lett.*, *30*(9), 1488, doi:10.1029/2002GL016828.

White, B. R. (1979), Soil transport by winds on Mars, *J. Geophys. Res.*, *84*, 4643–4651.

Wilson, R. J. (1997), A general circulation model simulation of the Martian polar warming, *Geophys. Res. Lett.*, *24*, 123–127.

Wilson, R. J. (2000), Evidence for diurnal period Kelvin waves in the Martian atmosphere from Mars Global Surveyor TES data, *Geophys. Res. Lett.*, *27*, 3889–3892.

Wilson, R. J., and K. Hamilton (1996), Comprehensive model simulations of thermal tides in the Martian atmosphere, *J. Atmos. Sci.*, *53*, 1290–1326.

Wilson, R. J., and M. I. Richardson (1999), Comparison of Mars GCM dust storm simulations with Viking mission observations, in *Fifth International Conference on Mars* [CD-ROM], *LPI Contrib. 972*, abstract 6234, Lunar and Planet. Inst., Houston, Tex.

Wilson, R. J., and M. I. Richardson (2000), The Martian atmosphere during the Viking mission, 1, Infrared measurements of atmospheric temperatures revisited, *Icarus*, *145*, 555–579.

Wilson, R. J., D. Banfield, B. J. Conrath, and M. D. Smith (2002), Traveling waves in the northern hemisphere of Mars, *Geophys. Res. Lett.*, *29*(14), 1684, doi:10.1029/2002GL014866.

Zurek, R. W., J. R. Barnes, R. M. Haberle, J. B. Pollack, J. E. Tillman, and C. B. Leovy (1992), Dynamics of the atmosphere of Mars, in *Mars*, edited by H. H. Kieffer, pp. 835–933, Univ. of Ariz. Press, Tucson.

S. Basu and M. I. Richardson, Division of Geological and Planetary Sciences, California Institute of Technology, MC 150-21 Caltech, 1200 East California Boulevard, Pasadena, CA 91125, USA. (shabari@gps.caltech.edu)

R. J. Wilson, Geophysical Fluid Dynamics Laboratory, National Oceanic and Atmospheric Administration, P.O. Box 308, Princeton, NJ 08542, USA.